JOURNAL OF GEOPHYSICAL RESEARCH, VOL. 102, NO. B3, PAGES 4933–4955, MARCH 10, 1997

Postseismic strain following the 1989 Loma Prieta earthquake from GPS and leveling measurements

Roland Bürgmann,[1] Paul Segall,[2] Mike Lisowski,[3] and Jerry Svarc[4]

Abstract. Postseismic deformation in the 5 years following the 1989 Loma Prieta earthquake has been measured with the Global Positioning System and precise leveling. Postearthquake velocities at distances greater than ~20 km from the coseismic rupture are not significantly different from those observed in the 20 years prior to the earthquake. However, velocities at stations within ~20 km of the rupture exceed preearthquake rates and exhibit unanticipated contraction normal to the strike of the San Andreas fault system. A combination of forward modeling and nonlinear optimization suggests that the observed postseismic deformations were caused by aseismic oblique reverse slip averaging 2.9 cm/yr on the San Andreas fault and/or the Loma Prieta rupture zone and 2.4 cm/yr reverse slip along a buried fault within the Foothills thrust belt. The best fitting sources of postseismic deformation are all located at depths of less than 15 km. We find no evidence for accelerated flow or shear below the Loma Prieta rupture in the first 5 years following the earthquake. The inferred postseismic slip is likely to have been caused by the coseismic stress change updip of the 1989 rupture.

Introduction

Geodetic measurements subsequent to some large earthquakes show accelerated strain rates in the years to decades following the rupture [e.g., *Thatcher*, 1986; *Pollitz and Sacks*, 1992]. For example, following the 1906 San Francisco earthquake, strain rates in the Point Reyes and Point Arena triangulation networks north of San Francisco were about 2-3 times the rates measured in the 1970s [*Thatcher*, 1974]. Postseismic transients have also followed subduction zone earthquakes in Japan [*Kasahara*, 1981; *Thatcher*, 1986].

Using simple models of postseismic relaxation, *Thatcher* [1974; 1983] concluded that existing deformation data can be explained by either the viscous relaxation of a ductile (asthenospheric) layer underlying an elastic (lithospheric) plate or by the downward propagation of aseismic slip along a lower crustal extension of the fault zone. Many mechanical models of deep-seated deformation transients following large dip-slip and strike-slip earthquakes have been proposed [*Bott and Dean*, 1973; *Nur and Mavko*, 1974; *Anderson*, 1975; *Budianski and Amazigo*, 1976; *Rundle and Jackson*, 1977; *Savage and Prescott*, 1978; *Cohen*, 1979; *Lehner et al.*, 1981; *Li and Rice*, 1987; *Pollitz*, 1992], however, there is a lack of adequate data to test and differentiate between them.

Fault creep at shallow depths (0 to 3 km) has been observed after several strike-slip earthquakes along the San Andreas fault (SAF) system. Shallow creep typically decays exponentially within a few years of the earthquake [*Smith and Wyss*, 1968; *Bilham*, 1989]. Postseismic accelerated creep at seismogenic depths has been inferred from trilateration measurements adjacent to seismic ruptures on the Calaveras fault in 1979 and 1984 [*Oppenheimer et al.*, 1990]. *Shen et al.* [1994] observed postseismic deformation with a relaxation time of about 34 days following the 1992 Landers earthquake. They suggest that slip on and below the rupture surface, as well as on secondary faults, best explains the observed motions.

Observations of historic seismicity patterns indicate that earthquakes tend to propagate along fault zones, rupturing fault segments immediately adjacent to and within several years of a previously active break. Examples involving strike-slip faults have been reported along the North Anatolian fault system [*Toksöz et al.*, 1979], in NE China preceding the 1975 Haicheng earthquake [*Scholz*, 1977], the Calaveras fault zone [*Oppenheimer et al.*, 1990], and the SAF zone [*Savage*, 1971; *Wood and Allen*, 1973]. In the 19th century, earthquakes along the SAF and the Hayward fault in the San Francisco Bay area occurred in clusters spread over several years [*Ellsworth*, 1990]. This suggests the existence of transient processes that occur with characteristic timescales of several years. Lacking geodetic data on the time-dependent deformation around previously ruptured fault segments, we can only speculate on the mechanics of postseismic deformation and the relation between strain transients and the clustering of earthquakes.

The *M* 7.1 Loma Prieta earthquake of October 17, 1989, occurred on a previously unrecognized fault plane along a restraining bend of the SAF zone (Figure 1). The earthquake ruptured a buried, 35-km-long fault dipping ~70° to the SW from about 8 to 18 km depth [*Dietz and Ellsworth*, 1990]. Strike slip and reverse dip slip of about 1.5 m are inferred from geodetic data [*Lisowski et al.*, 1990a; *Marshall et al.*, 1991; *Snay et al.*, 1991; *Williams et al.*, 1993]. The slip distribution is more complex in detail, with slip of up to 5 m occurring on two patches to the NW and the SE of the hypocenter [*Beroza*, 1991; *Hartzell et al.*, 1991; *Steidl et al.*, 1991; *Wald et al.*, 1991; *Arnadottir and Segall*, 1994; *Horton*, 1996].

Southwest dipping reverse faults northeast of the SAF, including the Monte Vista, Berrocal, and Shannon faults,

[1] Department of Geology, University of California, Davis.
[2] Department of Geophysics, Stanford University, Stanford, California.
[3] Hawaiian Volcano Observatory, U.S. Geological Survey, Hawaii National Park.
[4] U.S. Geological Survey, Menlo Park, California.

Paper number 96JB03171.
0148-0227/97/96JB-03171$09.00

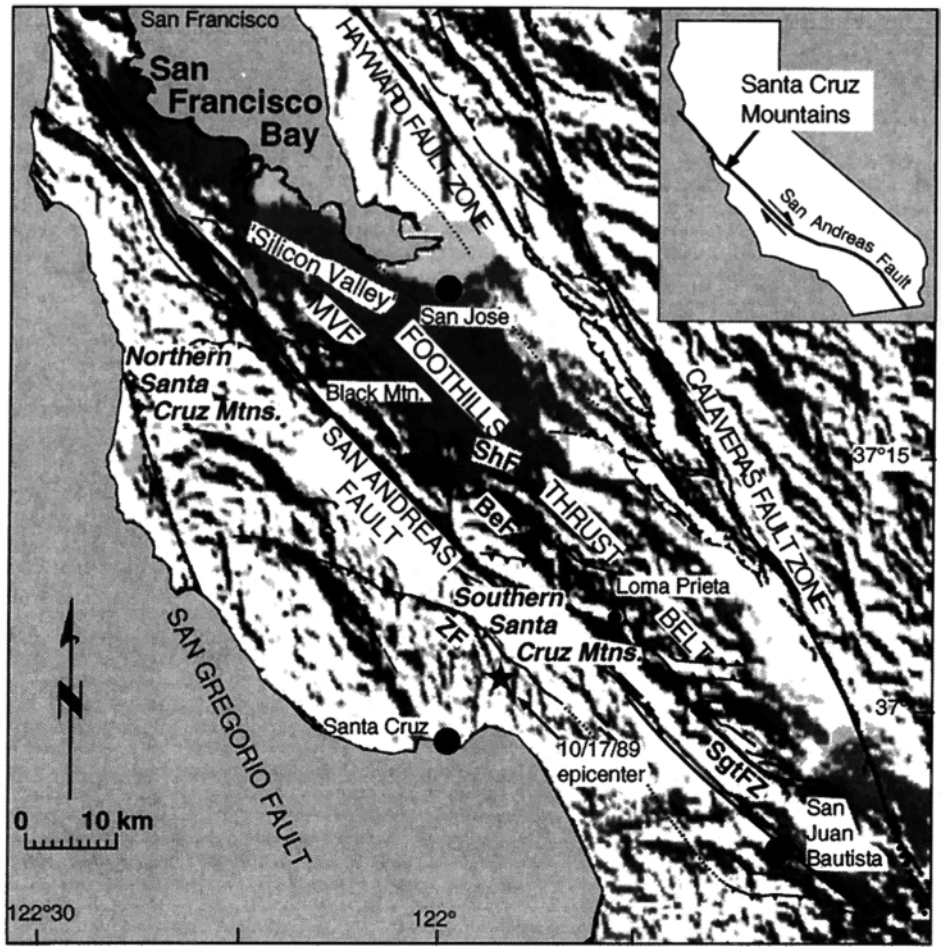

Figure 1. Fault map with shaded relief of the San Francisco Bay area showing major fault zones and localities described in text. Fault abbreviations are MVF, Monte Vista fault; ShF, Shannon fault; BeF, Berrocal fault; SgtFZ, Sargent fault zone; the Foothills thrust belt consists of the MVF, the BeF, and the ShF. Fault locations are from *Aydin and Page* [1984].

show evidence of Quaternary deformation (Figure 1) [*Aydin and Page*, 1984; *McLaughlin*, 1990; *Bürgmann et al.*, 1994; C.S. Hitchcock et al., unpublished data, 1994]. We refer to these faults collectively as the Foothills thrust belt. Broad zones of contractional surface deformation during the Loma Prieta earthquake follow the trend of these fault zones intermittently over a total distance of ~20 km, suggesting triggered slip [*Haugerud and Ellen*, 1990]. Triggered coseismic shallow slip was also recognized along the Sargent and San Andreas faults [*Aydin et al.*, 1992]. This zone has experienced strongly increased earthquake activity since the Loma Prieta event [*Reasenberg and Simpson*, 1992]. Focal mechanisms along the Foothills thrust belt show slip on reverse faults subparallel to the SAF [*Bürgmann et al.*, 1996].

Measurements of surficial postseismic slip subsequent to the Loma Prieta earthquake find shallow displacements along the SAF to be generally less than ~1 cm in the first year after the earthquake [*Behr et al.*, 1990; *Langbein*, 1990; *Rymer*, 1990]. The cumulative slip of aftershocks in the years subsequent to the earthquake (~5 mm [*King et al.*, 1990]) is too small to be detected geodetically. *Behr et al.* [1996] find that slip rates on the creeping section of the SAF near San Juan Bautista (Figure 1) accelerated from a preearthquake rate of 7-8 mm/yr to a rate of ~13 mm/yr since the earthquake. About 2-3 cm of excess slip occurred over the northernmost 15 km of the creeping section in the 3 years following the earthquake, probably down to a depth of 1-3 km [*Gwyther et al.*, 1992; *Behr et al.*, 1996]. Surficial creep rates on the southern Hayward and Calaveras faults decreased for about 3 years following the Loma Prieta earthquake [*Galehouse*, 1992; *Lienkaemper et al.*, 1992; J.J. Lienkaemper, personal communication, 1993].

In this study we present Global Positioning System (GPS) data collected between October 1989 and May 1994 from a number of geodetic networks (Figure 2). In this paper we refer to (1) the Black Mountain profile across the SAF 30 km NW of the Loma Prieta rupture [*Bürgmann et al.*, 1996], (2) the Loma Prieta profile through the epicentral region [*Savage et al.*, 1994], (3) the five-station Loma Prieta monitor network [*Davis et al.*, 1989; *Savage et al.*, 1994], and (4) the 22-station Santa Cruz Mountains network that was observed in March and April 1990 [*Snay et al.*, 1991; *Williams et al.*, 1993] and reoccupied in April and May 1994 (Figure 2 and Table 1). The Loma Prieta monitor network was surveyed with GPS and geodolite for several years prior to the earthquake [*Davis et al.*, 1989; *Lisowski et al.*, 1990b; *Savage and Lisowski*, 1995]. We also make use of velocities of two San Francisco Bay area very long baseline interferometry (VLBI)

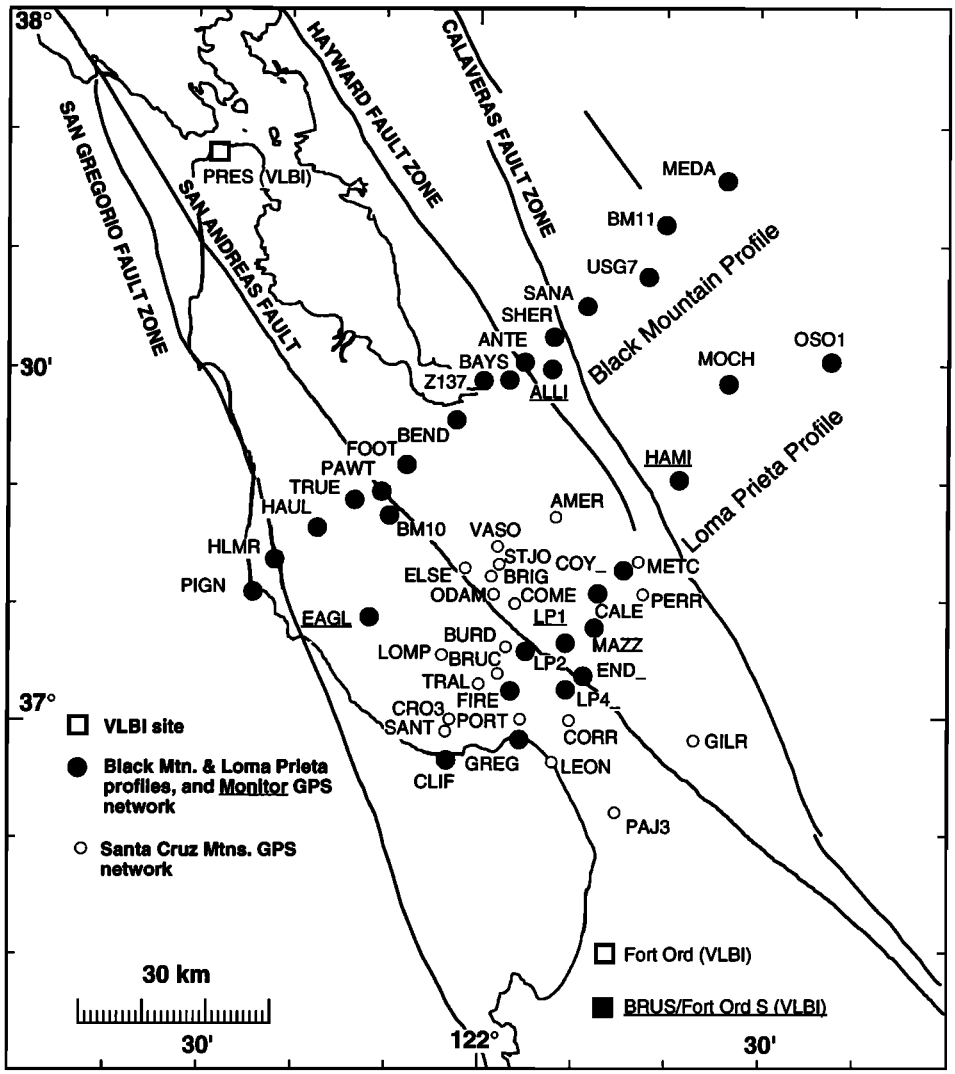

Figure 2. Post–Loma Prieta earthquake geodetic network in the southern San Francisco Bay area consisting of two fault crossing profiles, the Loma Prieta monitor network (station names underlined), the Santa Cruz Mountains network (open circles), and two very long baseline interferometry (VLBI) stations that were observed until 1991. Tables 1 and 2 summarize station coordinates and occupation times.

stations, determined relative to stable North America, for the time periods 1984 through 1989 and 1989 through 1991. VLBI observations at these sites were terminated in 1991 [*Argus and Lyzenga*, 1994]. Finally, high-precision vertical displacements are derived from a comparison of two occupations of a leveling line across the epicentral region of the Loma Prieta earthquake in March 1990 [*Marshall et al.*, 1991] and November 1992 [*Bürgmann et al.*, 1993]. Our objectives are to determine the amount, nature, and source of deformation following the Loma Prieta earthquake and to examine the consequences for the potential of future earthquakes on the peninsular SAF and other faults in the San Francisco Bay region.

GPS Data Collection, Processing, and Analysis

Data Collection

A total of 12 GPS surveys of the Black Mountain profile, 12 surveys of the Loma Prieta profile, and 19 surveys of the bay area monitor network were carried out between October 1989 and May 1994 (Figure 3 and Tables 1 and 2). Nine of these surveys included stations in both the Black Mountain and Loma Prieta profiles (usually LP1_ and BEND), allowing the relative coordinates of stations in both subnetworks to be accurately determined. In March and April 1990 the U.S. Geological Survey, the National Geodetic Survey, and Stanford University coordinated 2 weeks of GPS observations of both profiles, the monitor network, and 26 additional sites, referred to here as the Santa Cruz Mountains network, in order to constrain coseismic deformation during the 1989 earthquake [*Lisowski et al.*, 1990a; *Snay et al.*, 1991; *Williams et al.*, 1993]. In April and May 1994 we reoccupied 22 stations within the Santa Cruz Mountains network, together with the profile and monitor stations, to better resolve the spatial distribution of postseismic deformation.

Stations in the Loma Prieta profile and bay area monitor network were commonly observed once during each survey, whereas stations in the Black Mountain profile and Santa Cruz Mountains network were usually occupied at least twice in each

Table 1. Benchmarks Used in Postseismic GPS Survey and WGS-84 Coordinates

Station	Stamping	Latitude			Longitude		
		deg	arc min	arc sec	deg	arc min	arc sec
	Black Mountain Profile						
PIGN	PROP. COR. 1973	37	10	58.9	-122	23	40.3
HLMR	HALMAUR	37	13	42.2	-122	21	34.1
HAUL	HAUL 1989	37	16	25.4	-122	17	2.9
TRUE	TRUE 1990	37	18	44.2	-122	12	58.8
BM10	BMT10 RM1 1977	37	17	24.6	-122	9	12.2
PAWT	PAWT ERC BM1	37	19	28.2	-122	10	1.8
FOOT	FOOTHILL 1989	37	21	45.7	-122	7	23.8
BEND	BEND SURVEY PT 1987	37	25	34.8	-122	2	5.5
BAYS	BAYSHORE 1989	37	28	48.5	-121	56	55.1
BAYR	RM 1	37	28	48.5	-121	56	55.1
Z137	Z1370 1983	37	28	48.4	-121	58	25.2
ANTE	ANTELYNX 1989	37	30	24.2	-121	55	7.9
SHER	SHERIDAN 1989	37	32	28.7	-121	52	11.5
SANA	SAN ANT RES 1989	37	35	38.4	-121	48	35.8
USG7	USGS NO 7 784	37	37	18.5	-121	42	9.1
BM11	BM 112 ALAMEDA CO	37	41	39.3	-121	40	31.5
MEDA	MEDA 1946	37	45	19.1	-121	33	58.7
	Loma Prieta Monitor Network						
EAGL	EAGLE ROCK 1938 USE	37	8	49.0	-122	11	42.1
ALLI	ALLISON V A 2659	37	29	56.1	-121	52	16.7
HAMI	unstamped	37	20	30.2	-121	38	34.9
LP1_	LP1 891017	37	6	34.5	-121	50	40.7
BRUS	BRUSH 2 1978	36	35	23.2	-121	46	22.1
	Loma Prieta Profile						
CLIF	CLIFF 1931	36	56	59.1	-122	3	5.7
GREG	GREGOR 1989	36	58	56.2	-121	55	25.1
FIRE	FIRE 1989	37	2	49.0	-121	56	15.9
LP2_	SKYLAND 2	37	6	14.2	-121	54	31.4
LP4_	BUZZARD	37	3	0.2	-121	50	19.7
END_	END 1989 / nd	37	4	8.3	-121	48	32.4
LP1_	LP1 891017	37	6	34.5	-121	50	40.7
MAZZ	MAZZONE RM 1	37	8	13.0	-121	47	14.3
CALE	CALERO 1989 / ca	37	11	11.0	-121	46	57.5
COY_	COY 1989	37	13	9.2	-121	44	16.6
HAMI	unstamped	37	20	30.2	-121	38	34.9
MOCH	MOCHO 1875 1969	37	28	38.4	-121	33	21.4
OSO1	MT OSO NO. 1 1931	37	30	29.9	-121	22	30.1
	Santa Cruz Mountains Network						
AMER	AMERICAN 1947 1973	37	17	15.6	-121	51	57.3
BRIG	BRIGGS 1972	37	11	6.8	-121	59	46.0
BRUC	BRUCE 1972	37	4	23.1	-121	57	39.4
BURD	BURDETT 1972	37	6	37.0	-121	56	47.9
COME	COMEX 1972	37	10	0.7	-121	55	34.5
CORR	CORRALITOS 1947	37	0	41.8	-121	49	57.1
CRO3	CROWELL 1931 NO 3 1972	36	59	34.0	-122	3	7.9
ELSE	EL SERENO 1972	37	13	1.3	-122	1	21.9
GILR	GILROY NO 21984	36	58	47.2	-121	36	58.7
LEON	LEON 1931	36	56	46.0	-121	52	26.2
LOMA	LOMA PRIETA 1857 1958	37	6	39.6	-121	50	39.0
LOMP	LOMPICO 1947 1971	37	5	57.7	-122	3	32.0
METC	METCALF 1947	37	13	44.2	-121	42	49.9
NASA	NASA GSFC 7421	36	35	21.7	-121	46	19.7
ODAM	ODAMA 1972	37	10	49.2	-121	58	21.8
PAJ3	PAJARO 3 1977	36	52	44.5	-121	45	12.7
PERR	PERRYS 1946	37	11	1.6	-121	42	21.1
PORT	PORTER 1931	37	0	15.2	-121	55	11.7
SANT	unstamped	36	58	40.8	-122	3	21.3
STJO	ST JOSEPHS 1972	37	12	20.6	-121	58	36.6
TRAL	TRAILL 1972	37	3	31.0	-121	59	39.1
VASO	VASONA 1972	37	14	49.9	-121	57	58.4

survey (Table 2). Each station occupation commonly consisted of 6-8 hours of data collection; however, sites that could be left without an operator collected up to 24 hours of data per day. Tables 1 and 2 summarize the GPS data analyzed here. Table 1 presents the station codes, benchmark inscriptions, and station coordinates. Table 2 gives the occupation dates, GPS receiver types used, the agency that collected the field data, the fiducial stations used in the analysis (or source of precise orbit), and the networks occupied. For each survey with multiple occupations, Table 2 lists the day-to-day repeatability, expressed as the weighted root-mean-square in the north, east, and up directions.

Data Processing

Our GPS data analysis follows the methods described by *Davis et al.* [1989] and utilizes the Bernese GPS analysis software (version 3.5) [*Beutler et al.*, 1987; *Rothacher et al.*, 1990]. All data are processed with a satellite elevation cutoff angle of 15°, because higher or lower cutoff angles appear to reduce the short-term repeatability of the station coordinates. All data are first processed with an automatic cycle-slip fixing program. The double-difference carrier phase residuals are then visually inspected to remove remaining cycle slips and outliers. We attempt to resolve phase cycle ambiguities to integers by first resolving "wide-lane" ambiguities and then fixing the remaining linearly independent integer cycle ambiguities using the ionosphere-free linear combination. This combination of the two L band frequencies (L1 and L2) eliminates most first-order effects of dispersive ionospheric delays that affect longer baselines. Baselines shorter than 3 km that are not significantly affected by ionospheric variations are processed in the L1 frequency, which is less noisy than the L1-L2 combination. Practically all integer cycle ambiguities in the doubly differenced phase measurements are reduced to integer values in the local data. Atmospheric propagation delays are modeled with a zenith delay parameter at each station which is piecewise constant over ~3-hour periods.

Errors in the broadcast satellite ephemerides can be significantly reduced by monitoring the GPS satellites from a global network of tracking stations with well-known coordinates [e.g., *Larson et al.*, 1991]. For data collected prior to December 1991 we compute improved GPS satellite orbits utilizing data from North American fiducial stations (usually Mojave, California, Westford, Massachusetts, and Richmond, Florida) that are constrained to ITRF-92 coordinates and velocities. In a few surveys (see Table 2) we add data from tracking stations at Penticton and Yellowknife in Canada and from Kokee on Hawaii to compensate for the lack of data from the three principal fiducial stations. The tracking data are combined to solve for orbital parameters, solar radiation pressure, and "Y-bias" over 3- to 4-day arcs. We do not attempt to resolve integer phase ambiguities for baselines to or between tracking sites that are more than 600 km apart. For data collected from December 1991 through 1992 we utilize precise daily orbits computed by the Scripps GPS processing facility. Beginning in January 1993, we use precise International GPS Service (IGS) orbits [*Kouba*, 1995] and include data from the nearest IGS tracking sites (Quincy and DSSC10) in California. Final estimates of the local station coordinates, atmospheric zenith delay parameters, satellite orbit parameters (until December 1991), and synchronization errors are determined by processing the data from the fiducial stations, together with the ambiguity-fixed local data.

Data Precision and Accuracy

The precision of GPS measurements depends on the satellite and receiver clocks, propagation delays, satellite orbit and

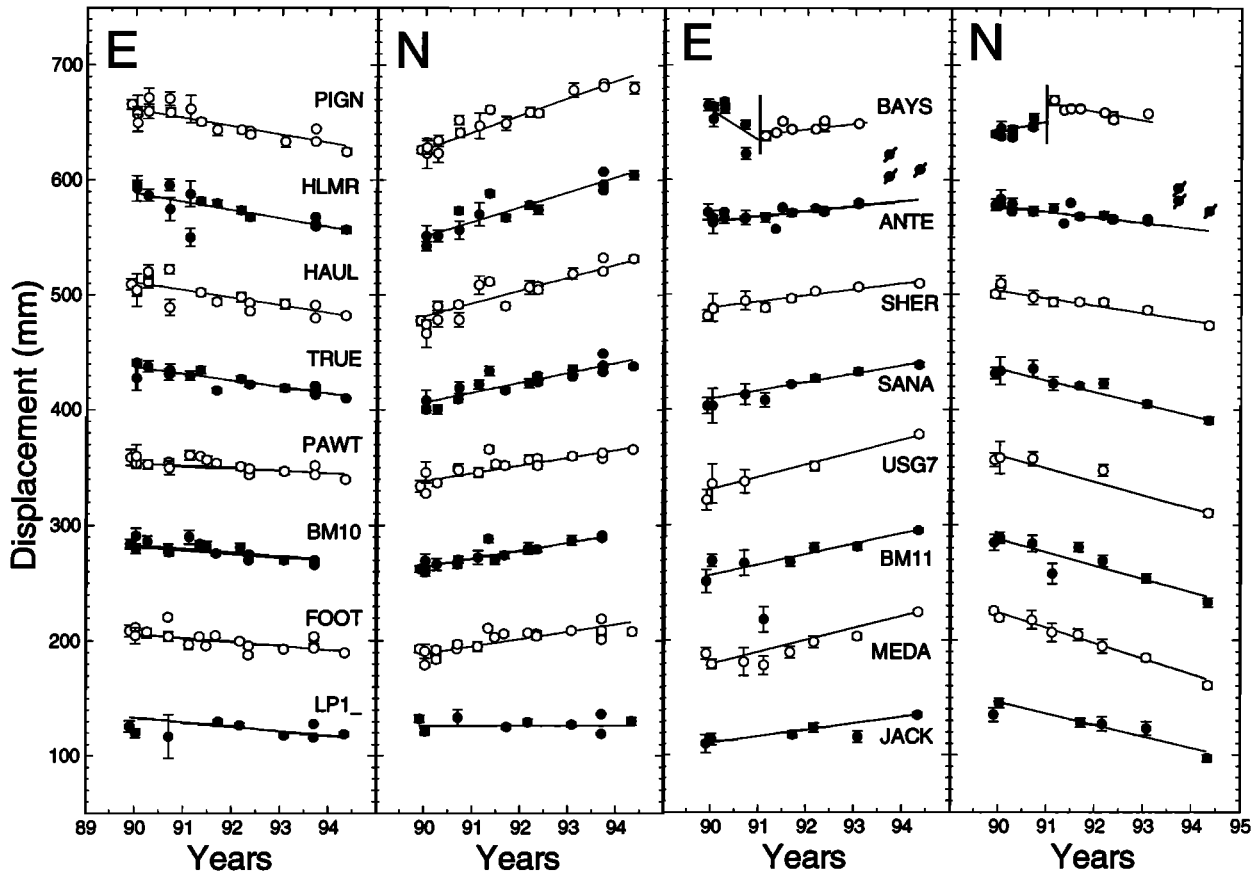

Figure 3a. Time series of relative changes in the horizontal (north and east) baseline components along the Black Mountain profile with respect to station BEND. The slope of the line fitted to the data is the relative station velocity.

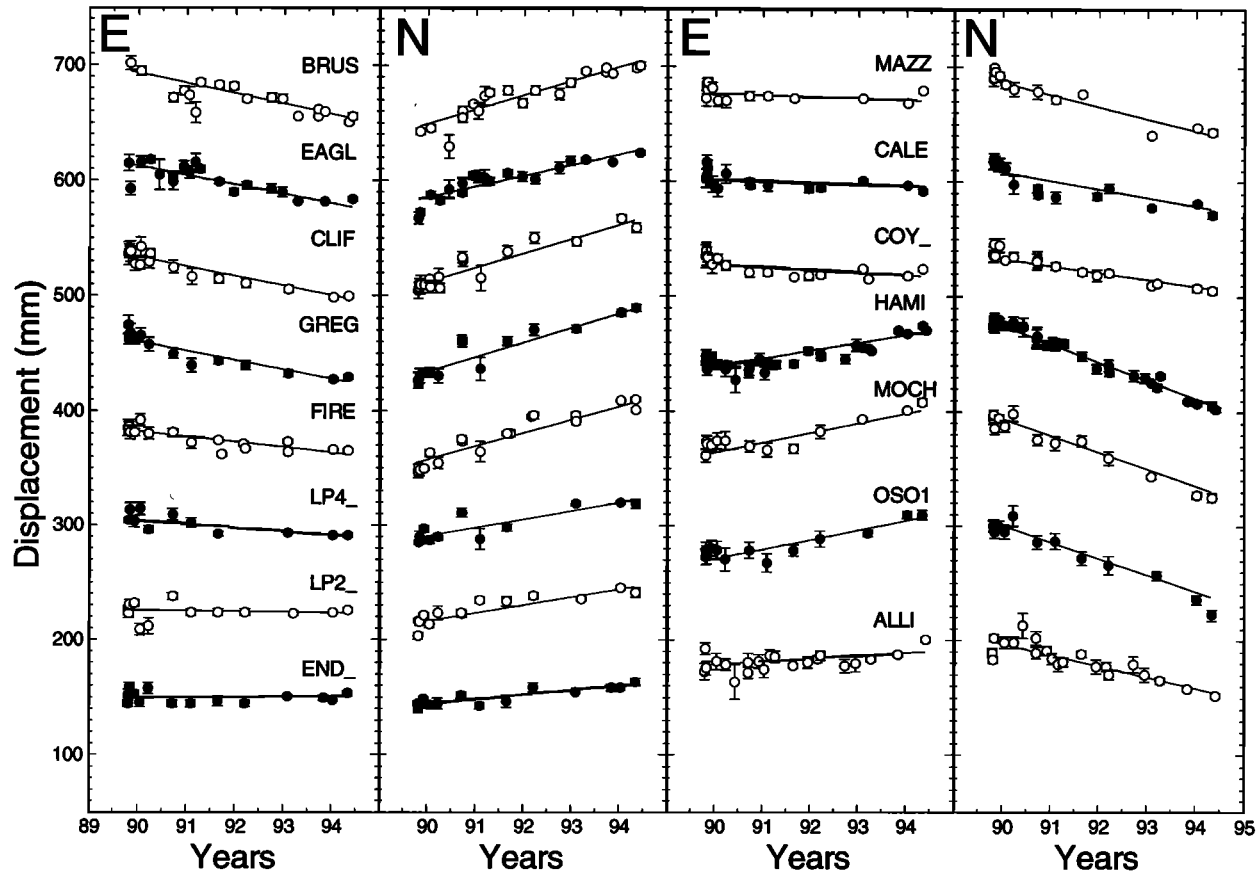

Figure 3b. Time series of horizontal coordinates of Loma Prieta profile and San Francisco Bay area monitor network stations relative to station LP1_.

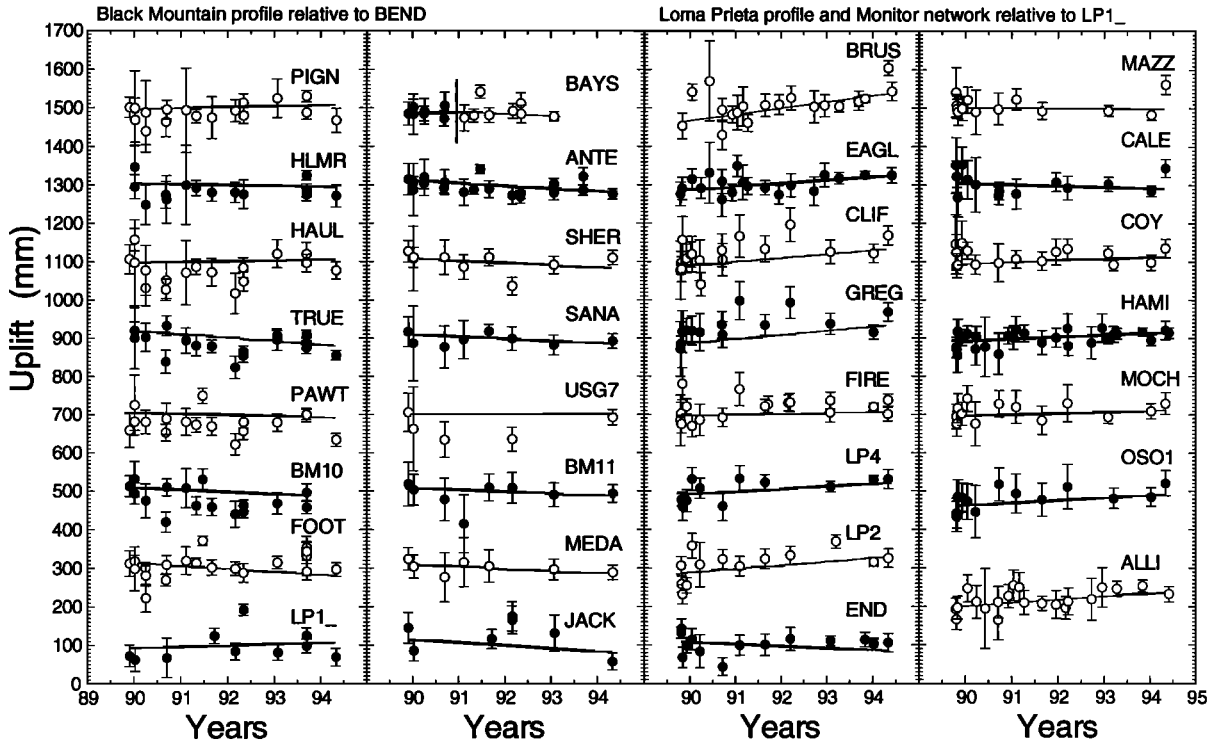

Figure 3c. Time series of vertical baseline component for Black Mountain profile stations relative to BEND and Loma Prieta profile and bay area monitor network sites relative to LP1_.

constellation characteristics, length and time of observation, the geographic location of a network, receiver types and post-processing software, set-up procedures, and stability of the monument.

Figure 3a shows changes in the north and east components of the station coordinates in the Black Mountain profile relative to BEND. In Figure 3b the time series of the sites in the Loma Prieta profile and the monitor network are shown relative to station LP1_ on Loma Prieta. Four receiver-station days are left out in the final computations as operators noted significant shifts in antenna positions during the surveys caused by bovine impact or tripod instability (occupations of HLMR in May 1992 and January 1993, ANTE in May 1992, and BAYS in January 1993). Between January and September 1993 our measurements indicate a horizontal offset of > 5cm of ANTE (Figure 3a). We assume that this motion was due to a disturbance of this site located in the curb of a residential road and do not use that data in our final velocity solution. Station BAYS in the Black Mountain profile was disturbed by vehicle impact in the fall of 1990. Following this, a tie between BAYS and a new reference mark BAYR was measured in December 1990. In May and June 1991 the old benchmark was surveyed, and the position of the reference mark at the time of these campaigns was calculated from the established tie. The reference mark was also disturbed in late 1992, and a new site Z137 was established nearby. Figure 3a shows the time series before and after the first benchmark disturbance determined by subtracting the BAYS-BAYR tie from the later measurements. Because the tie was measured after the disturbance, we cannot measure the true offset. Therefore the total displacement rate for BAYS is determined by solving for a common velocity of BAYS before the first incident, BAYS and BAYR from February 1991 to May 1992, and Z137 since 1992.

Table 2 summarizes the day-to-day repeatabilities achieved in campaigns including two or more site occupations. Between October 19 and November 1, three occupations of the Loma Prieta profile were conducted. In the June 1991, May 1992, and September 1993 Black Mountain profile campaigns most baselines were measured two to four times to estimate the precision of the survey results. Furthermore, the Black Mountain profile was measured within the same week with TI4100 and Trimble receivers in the January, April, and September campaigns of 1990. The Santa Cruz Mountains network sites were observed 2-14 times in 1990 and in 1994. We note apparent improvements in day-to-day repeatabilities from >10-hour observation times and in more recent surveys that benefited from better satellite coverage, receiver hardware, and the use of precise IGS orbits.

Postseismic Displacement Field From GPS

Least squares estimates of the relative station velocities are shown in Figure 3 as solid lines. A visual analysis of the time series along the Loma Prieta profile suggests a possible decay in the postseismic displacement rates for some stations. *Savage et al.* [1994] found that the decay was particularly evident in the SAF-normal component. Data collected in 1995 show that postseismic deformation rates had decayed to near pre-1989 values by 1993 [*Bürgmann et al.*, 1995]. While there is evidence for time-dependent deformation in some baselines, to first order the data can be fit with constant rates of motion. Because the data are irregularly sampled in time and the geometry of the active structures is not known a priori, it would be difficult to simultaneously solve for both fault geometry and time-dependent deformation history. In this paper we focus on determining the geometry of the source of postseismic defor-

Table 2. List of Experiments

Dates	Days	Receivers	Agency	Orbit Improvement	Network	Other Sites						Weighted RMS scatter, mm		
												North	East	Up
Oct. 19, 1989	9	4 TI	USGS	MOJA/RICH/WEST	LP, MON							3.2	4.0	11.5
Nov. 30, 1989	3	4 TI	USGS	MOJA/RICH/WEST	BM	HLMR*	LP1_							
Dec. 5, 1989	4	4 TI	USGS	MOJA/RICH/WEST	LP									
Jan. 7, 1990	5	4 SD, 4 TI	SU and USGS	MOJA/RICH/WEST/KOKE	BM							3.4	3.5	21.8
March 19, 1990	3	4 TI	USGS	MOJA/RICH/WEST/KOKE	LP									
March 20, 1990	15	5 TI	NGS	MOJA/RICH/WEST/KOKE	SCM							2.8	2.2	7.9
March 28, 1990	3	4 SD	SU	MOJA/RICH/WEST/KOKE		PORT†	LEON†	CROW†	TRAL†	CLIF†	PAJ3†			
March 30, 1990	1	4 TI	USGS	MOJA/RICH/WEST/KOKE	MON									
April 3, 1990	5	4 SD, 4 TI	SU and USGS	MOJA/RICH/WEST/KOKE	BM									
June 5, 1990	1	4 TI	USGS	MOJA/RICH/WEST	MON									
Sep. 11, 1990	5	4 SD, 4 TI	SU and USGS	MOJA/RICH/WEST	BM							2.9	5.8	11.6
Sep. 17, 1990	4	4 TI	USGS	MOJA/RICH/WEST	LP, MON	PIGN†	TRUE†	BM10†	BEND†					
Dec. 4, 1990	1	4 TI	USGS	MOJA/RICH/WEST	MON									
Jan. 15, 1991	1	4 TI	USGS	MOJA/RICH/WEST	MON									
Feb. 13, 1991	3	4 TI	USGS	MOJA/RICH/WEST	BM									
March 4, 1991	1	4 TI	USGS	MOJA/RICH/WEST	MON	HAMI*								
April 7, 1991	1	4 TI	USGS	MOJA/RICH/WEST	MON									
May 4, 1991	3	4 SST	SU	MOJA/RICH/WEST	BM	SHER*	SANA*	USG7*	BM11*	MEDA*	JACK*			
June 17, 1991	6	7 SST	SU	MOJA/RICH/WEST	BM	SHER*	SANA*	USG7*	BM11*	MEDA*	JACK*	6.5	6.9	24.9
				KOKE/YELL/PENT		BRUS†	CLIF†							
Aug. 26, 1991	4	6 AS	USGS	MOJA/RICH/WEST	LP, MON	HAMI*	CALE*							
Sep. 3, 1991	4	7 AS	USGS	Precise (Scripps)	BM	FIRE†								
Sep. 20, 1991	1	6 AS	USGS	Precise (Scripps)		LP1_†	FIRE†	BEND†	JACK†					
Dec. 17, 1991	1	6 AS	USGS	Precise (Scripps)	MON	CALE†	COY_†							
March 4, 1992	4	8 AS	USGS	Precise (Scripps)	BM	LP1_†	FIRE†	ALLI†						
March 17, 1992	3	8 AS	USGS	Precise (Scripps)	LP, MON									
May 6, 1992	6	4 SST	SU	Precise (Scripps)	BM	SHER*	SANA*	USG7*	BM11*	MEDA*	JACK*	2.0	3.3	10.0
Sep. 12, 1992	1	6 AS	USGS	Precise (Scripps)	MON	LOMA†								
Dec. 14, 1992	1	5 AS	USGS	Precise (Scripps)	MON									
Jan. 25, 1993	4	8 AS	USGS	Precise (IGS)	BM	LP1_†	FIRE†	ALLI†				3.4	3.3	18.0
Feb. 2, 1993	2	8 AS	USGS	Precise (Scripps)	LP									
March 17, 1993	1	5 AS	USGS	Precise (Scripps)		BEND†	ANTE†	BAYS†	Z137†					
March 18, 1993	1	5 AS	USGS	Precise (Scripps)		LP1_†	LP2_†	COY_†	OSO1†	HAMI†				
April 13, 1993	1	5 AS	USGS	Precise (Scripps)	MON									
Sep. 10, 1993	5	3 SSE/8 SST	SU	Precise (IGS)	BM	SHER*	SANA*	USG7*	BM11*	MEDA*	JACK*	3.1	3.4	8.8
						LP1_†	BRUS†	Z137†	CLIF†					
Oct. 26, 1993	2	6 AS	USGS	Precise (Scripps)	MON	END_†								
Jan. 11, 1994	2	8 AS	USGS	Precise (Scripps)	LP									
April 28, 1994	1	5 AS	USGS	Precise (IGS)		LP1_†	FIRE†	BEND†	JACK†					
April 30, 1994	15	8 SSE	SU/USGS	Precise (IGS)	BM, LP,SCM	BM10*	ALLI†	BRUS†				2.0	2.8	5.5
May 31, 1994	1	5 AS	USGS	Precise (Scripps)	MON									

Receiver abbreviations are TI, TI 4100; SD, Trimble 4000 SD; SST, Trimble 4000 SST; AS, Ashtech LM XII; and SSE, Trimble 4000 SSE. Agency abbreviations are USGS, U.S. Geological Survey; SU, Stanford University; and NGS, National Geodetic Survey. Orbit improvements are computed using the named fiducial stations or are from precise orbits. Networks are LP, Loma Prieta profile; MON, Loma Prieta monitor network; BM, Black Mountain profile; and SCM, Santa Cruz Mountains network.

* These are sites that were left out.

† These are additional sites.

mation. In a subsequent paper we will address the time dependence of strain.

We compute site velocities assuming linear motions over the 4.4-year time period. Coordinate estimates and covariance matrices for each observation file are combined to determine least squares estimates of station velocities. As appears to be the case in many GPS studies, we find that the formal errors computed during the GPS processing underestimate the observed scatter. The observed short-term repeatability and scatter about the best fitting linear displacement model suggest that the Bernese formal standard deviations must be scaled by a factor of 6 with computed orbits or a factor of 10 when using IGS orbits.

The station velocities relative to PAWT and their 95% confidence ellipses, using all data for all sites between October 1989 and May 1994, are shown in Figure 4. Note that the velocities of stations in the Santa Cruz Mountains network are based on only two surveys in March/April of 1990 and April/May of 1994. Figure 4 also shows the VLBI-derived velocities for the Pacific plate and the Sierra Nevada - Great Valley (SNGV) block (D. F. Argus and R. G. Gordon, written communication, 1996). A total of 41.3 ± 3 mm/yr relative motion between the SAF-bounding blocks occurs at this latitude (oriented N34.5°W ±2.5°) (D. F. Argus and R. G. Gordon, written communication 1996). The measured displacement rates of sites along the Black Mountain profile are consistent

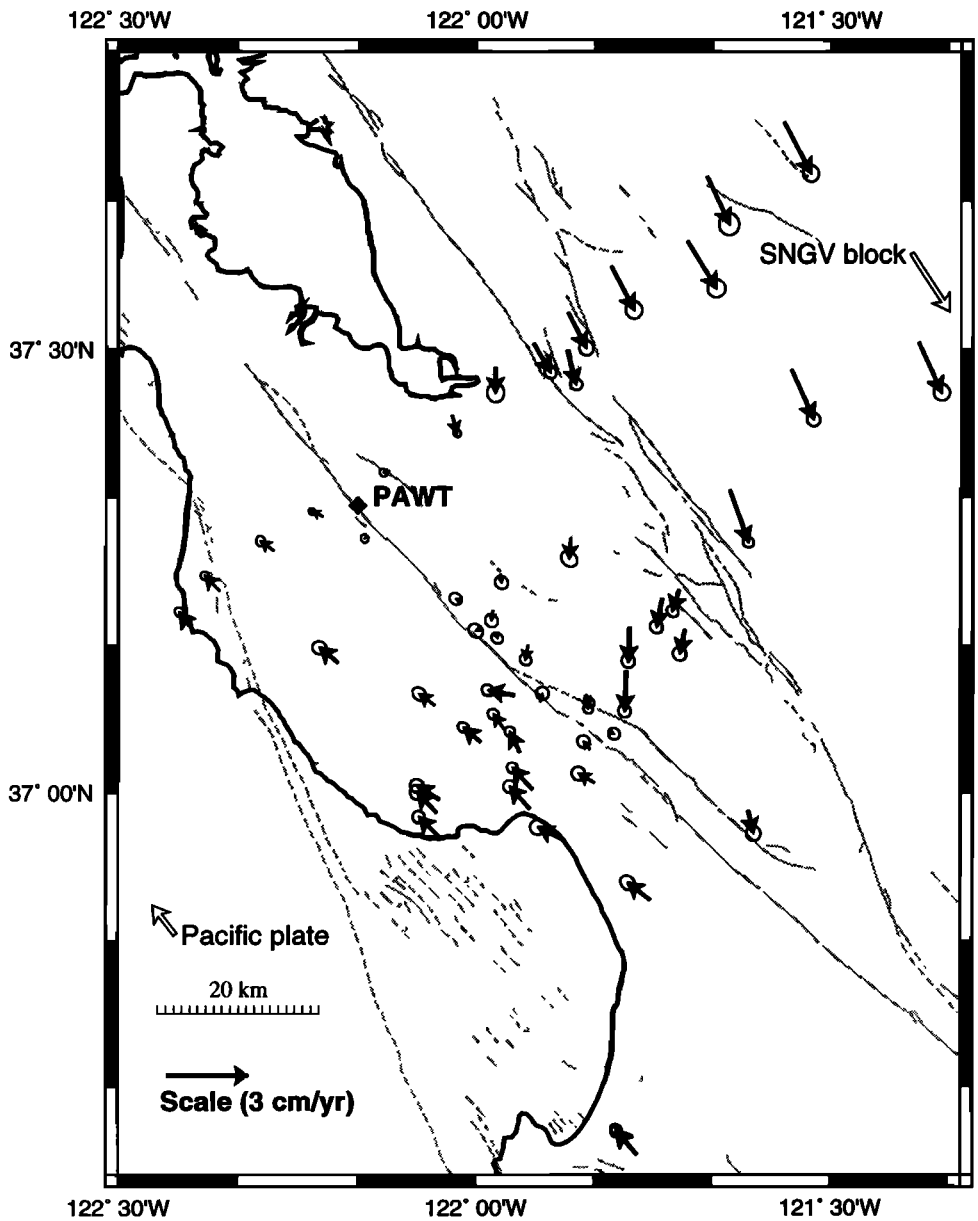

Figure 4. Postseismic velocity field computed from Global Positioning System (GPS) data collected between October 19, 1989, and May 31, 1994. Velocities and their 95% confidence ellipses are shown relative to station PAWT along the Black Mountain profile. Also shown are the plate velocities of the Pacific plate and the Sierra Nevada - Great Valley block determined from VLBI data (*AD.F. Argus*, written communication 1996). Most of the relative right-lateral plate motion occurs within our network. A zone of > 1 cm/yr contraction northeast of the San Andreas fault is the most apparent deviation from simple, distributed right-lateral shear.

Table 3. Preseismic and Postseismic Station Velocities Relative to Station PAWT

Station	Preseismic Model, mm/yr				Postseismic, mm/yr					
	East	+/-	North	+/-	East	+/-	North	+/-	Up	+/-
CLIF	-3.9	1.3	4.2	1.1	-7.9	1.0	8.0	1.0	6.0	6.5
GREG	-2.1	1.2	3.1	1.3	-7.9	1.0	8.6	1.0	3.9	6.8
FIRE	-1.3	1.2	2.1	1.1	-3.9	0.8	7.8	0.8	-9.5	5.5
LP4_	0.5	1.1	0.6	1.4	-2.3	1.0	2.9	1.0	-6.6	6.8
LP2_	0.3	1.0	0.6	1.1	0.9	1.0	3.0	1.0	-2.2	6.8
END_	1.5	1.1	-0.3	1.4	1.2	0.9	-0.5	0.9	-22.9	6.2
LP1_	1.7	1.0	-0.5	1.3	1.0	0.8	-4.9	0.7	-14.2	5.1
MAZZ	3.3	1.1	-1.8	1.6	-0.7	1.0	-15.1	1.0	-13.1	6.8
CALE	4.0	1.0	-2.6	1.6	-0.7	1.0	-12.8	1.1	-15.0	6.8
COY_	5.3	1.0	-3.9	1.9	-2.1	1.0	-10.8	1.0	-7.2	6.7
HAMI	13.1	1.3	-16.2	1.8	7.2	0.9	-20.1	0.8	-9.0	5.8
MOCH	13.2	1.3	-19.2	2.0	8.6	1.1	-19.0	1.1	-9.7	7.4
OSO1	13.2	1.3	-20.1	2.1	8.6	1.3	-19.1	1.3	-5.6	8.8
BRUS	-7.8	2.1	7.8	1.8	-7.7	0.8	9.8	0.8	14.3	5.7
EAGL	-3.0	0.8	3.1	0.7	-7.0	1.1	5.8	1.0	-4.4	7.3
ALLI	8.3	1.3	-11.6	1.3	3.4	1.0	-12.9	0.9	-10.9	6.2
PIGN	-3.3	0.8	3.3	1.3	-5.6	0.7	7.4	0.7	4.2	5.6
HLMR	-2.9	0.7	3.1	1.1	-5.5	0.6	5.9	0.6	-1.6	5.0
HAUL	-2.1	0.5	2.6	0.9	-5.0	0.7	3.7	0.8	5.2	6.6
TRUE	-1.0	0.3	1.2	0.4	-4.0	0.5	1.9	0.5	-9.8	4.1
BM10	-0.4	0.2	0.5	0.2	-1.2	0.6	-1.0	0.7	-3.3	4.9
FOOT	1.4	0.5	-1.6	0.4	-2.2	0.6	-0.3	0.6	-7.6	4.7
BEND	2.6	0.9	-3.7	0.7	2.0	0.6	-6.8	0.6	1.1	4.6
BAYS	3.2	1.7	-6.1	1.8	0.0	1.3	-9.6	1.5	8.4	5.7
ANTE	7.1	2.8	-11.0	1.7	6.5	0.9	-11.0	1.0	-4.6	7.0
SHER	8.8	1.4	-12.9	1.6	6.9	1.1	-13.6	1.2	-4.1	8.4
SANA	10.5	1.5	-15.9	1.5	8.8	1.3	-16.9	1.4	0.7	9.9
USG7	11.5	1.5	-17.7	1.7	11.0	1.4	-18.1	1.4	6.2	9.9
BM11	11.5	1.5	-18.4	1.7	8.5	1.6	-18.3	1.7	0.3	12.1
MEDA	11.4	1.6	-19.3	1.8	10.4	1.2	-19.7	1.3	-1.8	9.0
JACK	7.1	1.6	-13.1	1.6	6.3	1.6	-16.8	1.6	-4.8	10.4
LOMA	1.7	1.0	-0.6	1.3	1.2	0.8	-2.9	0.8	7.4	5.7
BRIG	0.5	0.7	0.1	0.7	-1.3	1.1	-0.6	1.1	10.0	7.8
METC	6.0	1.1	-4.8	2.0	-2.5	0.9	-8.1	0.9	10.4	6.2
PERR	5.5	1.0	-4.1	1.9	-1.9	1.1	-9.2	1.0	21.9	7.2
PORT	-1.7	1.2	2.7	1.2	-7.8	0.9	8.4	0.8	14.2	5.7
STJO	1.3	0.7	-0.7	0.8	-0.6	1.0	-3.8	1.0	8.7	6.7
TRAL	-2.1	1.2	2.5	1.0	-6.5	0.8	5.6	0.8	14.3	5.4
ELSE	0.7	0.6	-0.2	0.6	-1.8	1.0	0.8	0.9	11.9	6.2
LEON	-2.2	1.2	3.4	1.5	-10.3	1.2	5.2	1.2	18.6	8.4
AMER	3.9	1.0	-3.4	1.4	-0.7	1.3	-8.0	1.2	15.5	8.5
BRUC	-1.3	1.2	1.9	1.1	-4.0	0.9	5.6	0.8	14.0	5.9
SANT	-3.6	1.2	3.8	1.1	-7.3	1.1	7.9	1.2	18.1	8.2
VASO	2.1	0.7	-1.8	0.8	0.4	1.0	-3.2	1.0	11.5	6.9
CORR	-0.4	1.2	1.5	1.5	-5.9	1.1	3.6	1.1	14.5	7.3
PAJ3	-3.1	1.4	3.7	1.9	-8.5	1.1	6.7	1.1	10.4	8.0
BURD	-0.3	1.0	1.1	1.0	-10.1	0.9	2.1	0.9	19.7	6.4
CRO3	-3.5	1.2	3.7	1.0	-8.4	1.1	5.3	1.1	17.9	7.0
NASA	-7.9	2.1	7.8	1.8	-7.9	0.9	8.7	0.8	16.9	5.6
LOMP	-2.4	1.1	2.6	0.8	-5.8	1.1	4.4	1.1	-3.2	9.3
COME	1.4	0.9	-0.6	1.0	-1.0	0.9	-5.6	0.9	29.5	7.6
ODAM	0.8	0.8	-0.2	0.8	0.5	0.9	-1.8	0.9	9.7	6.1
GILR	5.8	1.4	-4.0	1.8	2.2	1.2	-8.7	1.2	-25.4	16.7

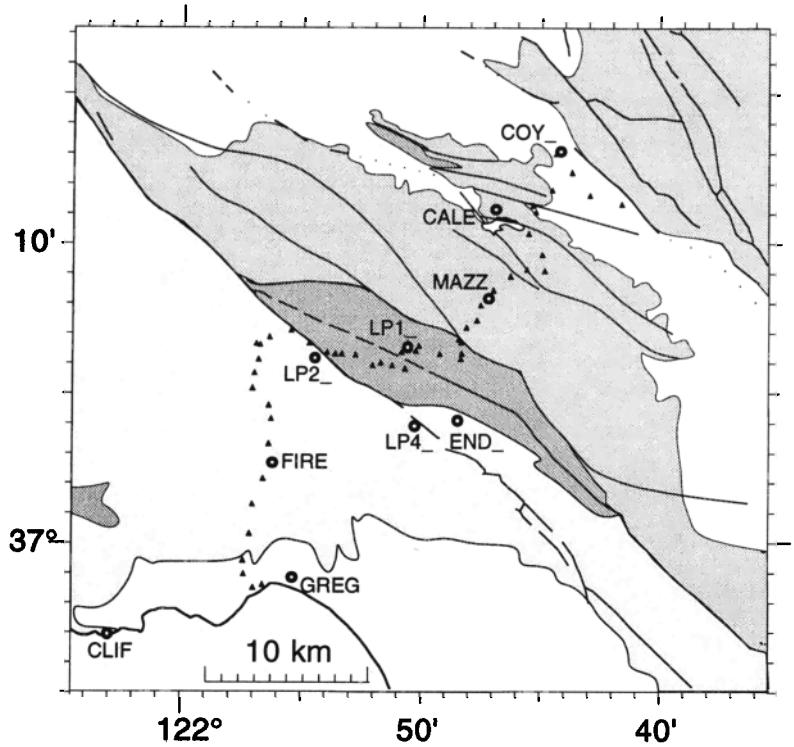

Figure 5. Schematic geologic map of southern San Francisco Bay area showing the location of benchmarks (triangles) of the leveling line. Sites on bedrock (shaded patterns) are not significantly influenced by groundwater level changes. Also shown are the locations of the nearby GPS stations of the Loma Prieta profile (circles).

with right-lateral shear across the SAF system. About 32 mm/yr of right-lateral motion is accommodated across the 100-km width of this profile. Velocities of sites along the Loma Prieta profile and in the Santa Cruz Mountains network are also consistent with broadly distributed right-lateral shear, except for the region between Loma Prieta and the Calaveras fault zone, where sites move almost due south relative to PAWT. The sense of shear is left lateral between MAZZ and METC. Between OSO1 and BRUS the network accommodates 34 mm/yr of right-lateral shear directed N32°W.

The scatter in the vertical component is several times greater than in the horizontal. Figure 3c shows the time series for the relative elevation changes of the stations along the two profiles and the monitor network. We find that only few vertical displacement rates are formally significant at the 2σ level, and even these should be viewed with caution. We include the GPS-derived vertical motions in our analysis; however, because of their large uncertainties, they do not influence our results strongly.

Leveling Data and Analysis

The low vertical precision (1-3 cm) in the GPS data did not allow us to resolve significant vertical motions (Table 3). Vertical motions can help to resolve between competing models of postseismic deformation, as discussed below. For this reason, a leveling line across the epicentral area of the 1989 Loma Prieta earthquake [*Marshall et al.*, [1991, Line 4] (Figure 5) was resurveyed to measure postseismic elevation changes [*Bürgmann*, 1993; *Bürgmann et al.*, 1993].

The leveling line is part of a larger network that was last occupied in the spring of 1990 to determine coseismic elevation changes [*Marshall et al.*, 1991]. First-order, single-run leveling surveys were performed by the National Geodetic Survey (NGS) in February and March 1990 and in November 1992. The line extends from Capitola at the Pacific coast via Loma Prieta to Coyote in the central Santa Clara valley, roughly parallel to the Loma Prieta GPS profile. The leveling line spans much of the width of the zone of anomalous fault-normal displacements determined from GPS. The only preearthquake occupation of this line occurred in 1953 [*Marshall et al.*, 1991].

A detailed analysis of the data and associated errors shows that the measured displacements are significant and apparently of tectonic origin [*Bürgmann*, 1993]. The data are corrected (by up to 4 mm) for systematic errors due to level collimation, rod calibration, thermal expansion of the rod tapes, Earth tides and associated gravitational effects, and atmospheric refraction by the NGS. The elevation changes between 1990 and 1992 are listed as the differences of the normal orthometric heights relative to the southwesternmost benchmark in Table 4 and are shown in Figure 6. Data from three apparently unstable benchmarks (stations HS5204, HS5213, and HS 5235 in Table 4) were discarded in the following analysis.

Random error is expected to accumulate with the square root of distance and was estimated as 0.8 mm/(km)$^{1/2}$ for the 1990 survey based on double-run sections [*Marshall et al.*, 1991]. The corresponding error of the 1992 survey is 0.65 mm/(km)$^{1/2}$ based on 10 double-run sections. Random error estimates based on the observed misclosure of circuits that

Table 4. Postseismic Elevation Changes Along Line 4 Across Loma Prieta

Acronym	Normal Designation	Latitude			Longitude			Survey Distance	Orthometric Height 1992,	1992-1990,
		deg	arc min	arc sec	deg	arc min	arc sec	km	m	mm
GU2285	M 1237	36	58	53	121	56	11	0.85	22.7060	-2.02
GU2286	N 1237	36	58	37	121	56	35	0.00	24.6180	0.00
GU2287	Z 212	36	58	31	121	56	58	0.54	19.4696	0.86
GU2290	P 1237	36	58	23	121	57	10	1.01	16.5193	2.60
GU4168	N 1456	36	58	59	121	57	22	1.63	10.9074	3.72
GU4169	32 WLS	36	59	26	121	57	24	2.47	12.5871	3.23
HS5194	P 1456	37	0	19	121	57	8	4.08	32.4363	3.48
HS5195	Q 1456	37	1	18	121	57	1	6.09	63.0128	3.22
HS5196	CHISELED SQUARE A	37	2	9	121	56	35	7.89	69.6912	3.32
HS5197	R 1456	37	2	44	121	56	18	9.12	70.7524	-0.12
HS5198	S 1456	37	3	19	121	56	21	10.31	80.9344	4.43
HS5199	T 1456	37	4	9	121	56	15	12.02	141.7645	6.43
HS5200	U 1456	37	4	36	121	56	21	12.86	176.5290	10.26
HS5201	1940	37	5	1	121	56	57	14.16	253.9460	13.55
HS5202	28 WLS	37	5	41	121	56	57	15.53	339.1622	13.21
HS5203	CHISELED SQUARE B	37	6	8	121	56	47	16.45	394.0883	23.41
HS5210	Z 1456	37	6	39	121	56	52	17.76	437.1345	21.01
HS5204	BURDETT	37	6	37	121	56	43	18.06	458.0249	4.42
HS5205	27 WLS	37	6	52	121	56	20	18.76	471.7535	16.74
HS5206	V 1456	37	7	6	121	55	26	20.21	477.2755	11.84
HS5207	W 1456	37	6	40	121	54	40	21.61	548.6984	11.84
HS5208	X 1456	37	6	22	121	53	56	22.91	572.6101	6.25
HS5209	Y 1456	37	6	19	121	53	36	23.59	609.2242	6.21
HS5211	A 1457	37	6	19	121	53	20	24.46	687.6756	4.31
HS5212	B 1457	37	6	17	121	52	45	25.39	762.6576	7.22
HS5213	C 1457	37	5	56	121	52	2	26.77	768.5816	-5.93
HS5214	D 1457	37	6	1	121	51	42	27.45	844.0607	12.75
HS5215	E 1457	37	5	56	121	51	13	28.06	906.5542	12.67
HS5216	F 1457	37	5	49	121	50	41	29.12	939.1038	12.04
HS5217	G 1457	37	6	22	121	50	49	30.50	1024.9336	11.68
HS5218	LOMA PRIETA RESET	37	6	39	121	50	38	31.95	1154.1363	8.68
HS5219	LOMA	37	6	41	121	50	35	31.97	1154.7195	10.40
HS5220/LP1	LOMA PRIETA 1	37	6	35	121	50	37	32.13	1152.2434	7.90
HS5221	H 1457	37	6	25	121	50	14	31.51	906.7855	7.49
HS5222	J 1457	37	6	35	121	50	6	31.97	870.7284	8.80
HS5223	K 1457	37	6	18	121	49	14	33.50	788.3253	5.26
HS5224	HJH 55	37	6	9	121	48	20	34.91	728.1352	1.93
HS5225	L 1457	37	6	19	121	48	18	35.70	600.7683	-1.48
HS5226	M 1457	37	6	41	121	48	19	36.52	480.6714	-7.92
HS5227	N 1457	37	6	47	121	48	25	37.59	364.0149	-7.39
HS5228	P 1457	37	7	11	121	48	6	38.71	300.7025	-17.70
HS5230	Q 1457	37	7	25	121	47	40	39.81	279.0617	-18.29
HS5229	ANGLE IRON	37	7	25	121	47	39	39.82	276.6817	-18.66
HS5231	HJH 53	37	7	56	121	47	30	40.91	246.2474	-20.28
HS5232	R 1457	37	8	26	121	46	58	42.34	227.6313	-21.64
HS5233	CHISELED SQUARE C	37	8	54	121	46	15	43.83	207.0110	-20.22
HS5234	S 1457	37	9	7	121	45	35	44.98	203.2404	-21.88
HS5235	SPIKE	37	9	7	121	45	35	45.01	201.8287	-32.57
HS5236	T 1457	37	9	5	121	44	49	46.25	191.4214	-23.77
HS5237	U 1457	37	9	37	121	44	56	47.28	230.5187	-25.24
HS5239	HJH 51	37	10	20	121	45	30	48.98	156.2777	-26.88
HS5240	V 1457	37	11	3	121	45	12	50.86	145.6818	-28.85
HS5241	W 1457	37	11	16	121	45	19	51.57	94.4624	-31.73
HS5242	X 1457	37	11	47	121	44	31	53.08	76.8338	-32.99
HS2775	L 174	37	12	22	121	43	41	54.74	79.7462	-37.71
HS2776	P 19	37	13	0	121	44	21	56.29	77.5943	-36.48
HS2773	Y 176	37	11	39	121	42	56	56.48	88.5071	-39.85
HS5407	HPGN CA 04 03	37	11	20	121	41	38	58.86	102.2432	-

included line 4 in 1990 are 2.5 mm/(km)$^{1/2}$ [*Marshall et al.*, 1991]; however, it is not possible to know how much line 4 itself contributes to the misclosure.

Slope-dependent systematic errors may be caused by errors in the rod calibrations. We test for the accumulation of elevation-dependent errors by performing an unweighted least squares fit of geodetic tilt to topographic slope along individual sections [*Stein*, 1981]. The correlation is not significant at the 95% level [*Bürgmann*, 1993]. A rough correspondence between elevation change and topography is apparent in Figure 6 on the eastern flank of the southern Santa Cruz Mountains. Because this correlation is not observed on the

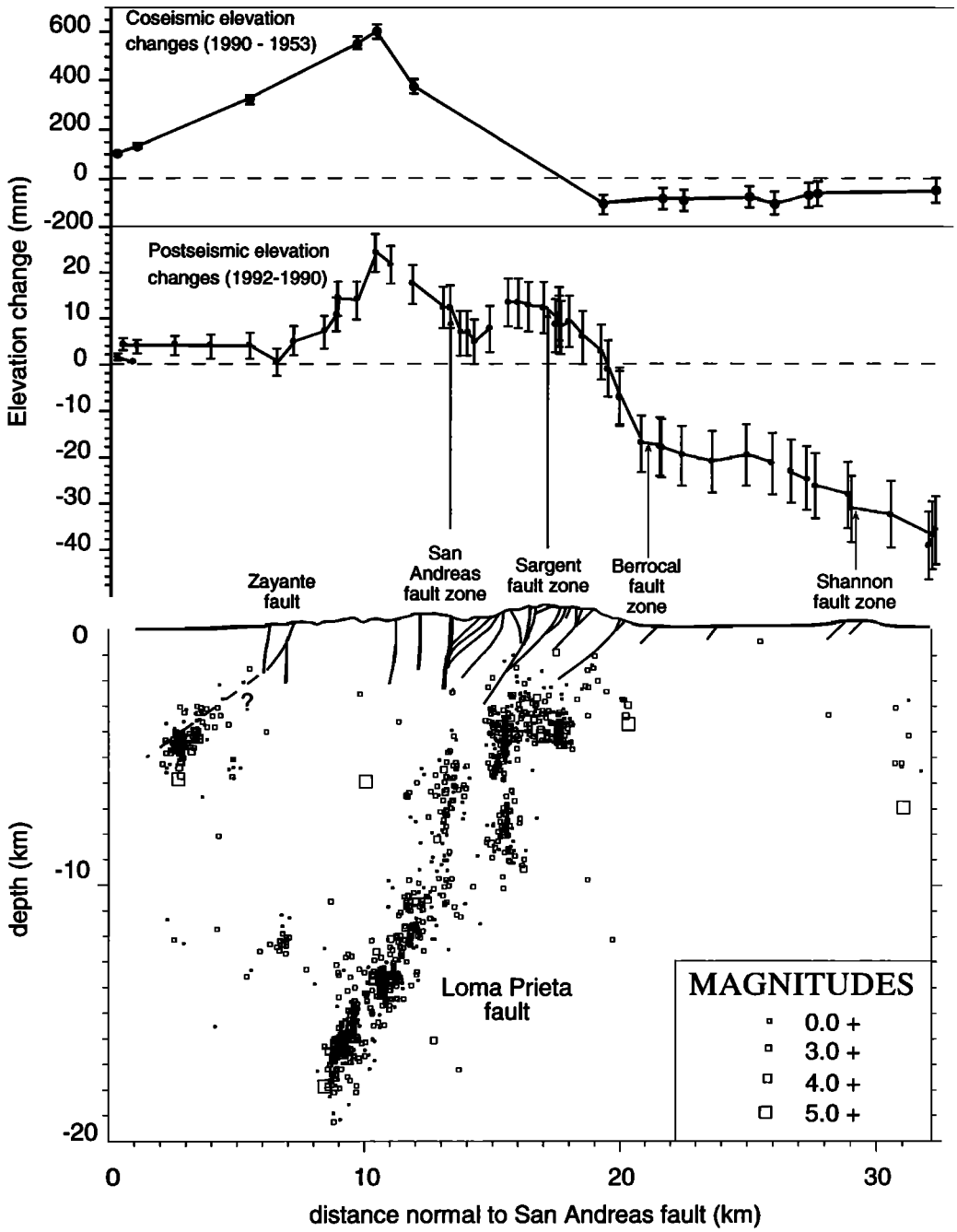

Figure 6. Postseismic elevation changes along the leveling line from SW to NE. The error bars represent the error in elevation change relative to the southwestern end of the baseline near Capitola. Also shown is a structural cross section across the San Andreas fault (SAF) and the Foothills thrust belt (modified from *McLaughlin* [1990]) and Loma Prieta aftershocks. The plotted earthquakes are from a 15-km-wide zone centered on the cross section and include all well-located events from 1 month after the Loma Prieta earthquake until December 1992. Note that the steepest gradient in the elevation changes is located in the hanging wall of the Berrocal fault. The Berrocal fault zone also appears to be associated with high aftershock activity. The coseismic elevation changes [from *Marshall et al.*, 1991] on this line are shown for comparison.

remainder of the line, we suggest that this is due to thrust faulting along the Foothills thrust system (see below) rather than measurement error.

The five northeasternmost stations along line 4 are located in unconsolidated Santa Clara Valley sediments. They may be affected by well water withdrawal and seasonal changes in water level. A detailed analysis of historic leveling data in the area and well water records shows that water-induced subsidence is not a significant problem for these benchmarks [*Bürgmann*, 1993].

Assuming that the errors of the two campaigns are not correlated, the relative uncertainty in the elevation change is $\delta_i^2 = \alpha_1^2 + \alpha_2^2$, where α_1 and α_2 are the random errors in millimeters per square root kilometer determined for the two

surveys. The random errors thus accumulate with distance along the line at a rate of $\delta = 1$ mm/(km)$^{1/2}$.

The signal to noise ratio of the leveling data is

$$\left[\frac{d^T\Sigma^{-1}d}{N}\right]^{1/2} = 3.2.$$

Here d is the $N\times1$ vector of the elevation changes, Σ is the data covariance matrix, and $N = 46$ are the total number of sections used. This value compares with the signal to noise ratio of 9.3 of the coseismic uplift along line 4 that had very large elevation changes but that also had much larger associated errors [*Marshall et al.*, 1991].

Pre–Loma Prieta Earthquake Displacement Field

The velocity field shown in Figure 4 includes interseismic, as well as postseismic, motions. To isolate the deformation associated purely with post-1989 processes, we first construct a model of the interseismic (preearthquake) velocity field and subtract it from the measured velocities in Figure 4. The interseismic model is based on pre-1989 geodetic observations. Trilateration measurements in the San Francisco Bay area have been carried out for two decades prior to the Loma Prieta earthquake [*Lisowski et al.*, 1991]. Rigid-body rotations of the network are constrained by GPS observations at trilateration stations (or by ties between nearby GPS and trilateration marks) at LP1_, EAGL, ALLI, HAMI, and BRUS (Figure 2). Except for the effects of the 1979 Coyote Lake and 1984 Morgan Hill earthquakes, the deformation rates appear to have been constant during that time period. Figure 7 shows the horizontal velocity field in the region based on 20 years of trilateration data and up to 5 years of GPS data from the five Loma Prieta monitor stations (solid arrows) relative to Loma Prieta. Open arrows represent the velocities predicted by a dislocation model of bay area strike-slip faults discussed below. Gray bold lines indicate the surface projection of the model strike-slip faults.

The interseismic velocity field in the southern San Francisco Bay area accommodates 38 ± 5 mm/yr of right-lateral motion across a zone about 120 km wide, as described by *Lisowski et al.* [1991]. The velocity vectors are approxi-

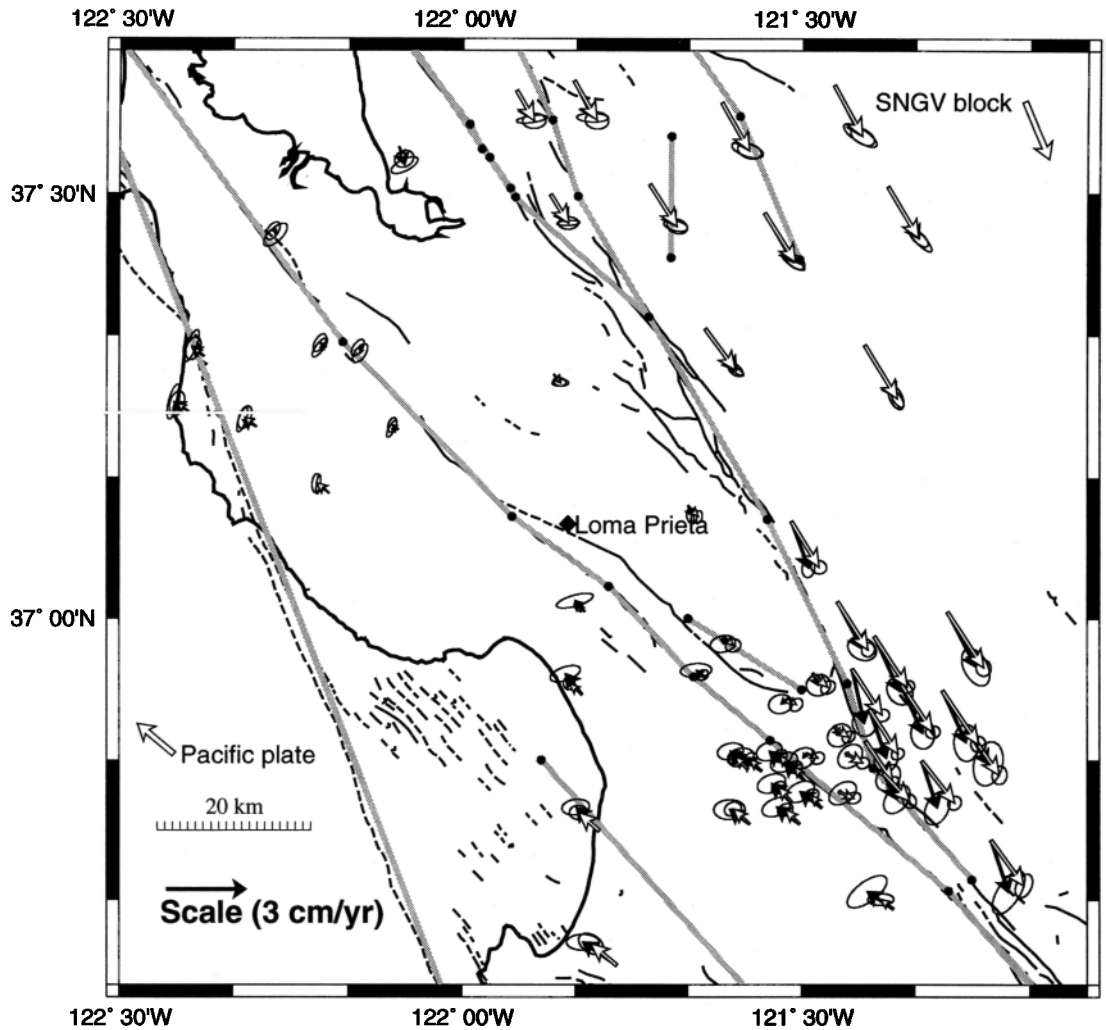

Figure 7. Comparison of pre–Loma Prieta earthquake site velocities with 95% confidence ellipses (solid arrows) and velocities computed from an elastic model (open arrows) derived by linear inversion of the preseismic data. All displacements are shown relative to Loma Prieta. Shaded lines indicate the surface projection of the dislocation elements of the interseismic model.

mately parallel to the regional trend of the SAF system and do not appear to be influenced by the local left bend in the SAF trace through the Santa Cruz Mountains. The displacement field broadens significantly from San Juan Bautista toward the northwest.

Figure 8 shows a close-up view of the measured pre-earthquake (open arrows relative to BMT RF) and postseismic (solid arrows relative to PAWT) motions. Only a few of the postseismic stations were surveyed before the Loma Prieta earthquake. At some of the stations for which both pre- and postseismic data exist, such as HAMI, AMER, and GILR, the postseismic velocities exhibit significant fault-normal convergence that is not observed in the preseismic velocities. In order to compare preearthquake and postearthquake velocities at the remainder of the GPS stations, we must interpolate the preearthquake velocity field between stations. To do so, we developed a dislocation model of the San Francisco Bay area [*Bürgmann et al.*, 1996]. Uniform-slip dislocations in an elastic, homogenous, and isotropic half-space represent the bay area faults. In this model, interseismic shear about a locked strike-slip fault is approximated by slip on a buried fault plane below the seismic zone at a rate comparable to the average geologic slip rate [*Savage and Burford*, 1970; *Lisowski et al.*, 1991]. Surface creep on the Hayward, Calaveras, and the central SAF is modeled by shallow fault elements.

We estimate fault slip rates using a linear inversion method [*Du et al.*, 1992] that uses the trilateration and GPS data to estimate slip on 78 individual segments of the bay area faults. Note that our primary objective here is to simply develop an approximation of the preseismic velocity field which can be used to compute the expected motions of stations for which preseismic data are not available. All faults are assumed to be vertical with pure strike-slip offset. A priori estimates of slip rate are taken from *Lienkamper et al.*'s [1992] compilation of geologically determined slip rates. Results of the inversion indicate (1) deep (> 15 km) slip on the peninsular segment of the SAF at about 15-20 mm/yr, (2) deep slip (> 11 km) on the Hayward fault at 15 ± 3 mm/yr, (3) deep slip (> 10 km) on the northern Calaveras fault at about 10-12 mm/yr and at up to 35 mm/yr on the southern Calaveras fault, and (4) shallow creep on the East Bay faults and the SAF south of San Juan Bautista at rates comparable to the a priori values. For the San Gregorio fault we compute 2 ± 1 mm/yr slip from 10 to 15 km depth. Below 15 km the model predicts insignificant left-lateral slip (0.7 ± 1 mm/yr). The deep slip rate on the southern Calaveras fault is clearly too high and may be related to unaccounted for effects of the Coyote Lake and Morgan Hill earthquakes.

Figure 7 compares the measured and modeled station velocities relative to Loma Prieta. Formal uncertainties in the predicted velocities are computed from the uncertainty in the data. Because the inversion constrains the predicted velocities to be generated from slip in an elastic half-space, the uncertainties in the predicted velocities are actually less than the uncertainties in the observed velocities. We thus scale the uncertainties in the predicted velocity field, by roughly a factor of 3, so that the predicted motions are not better determined than the observations.

In general, the model predicts the observed velocity field quite well. The only significant exception is along the southern Calaveras fault in the Hollister network. Stations just

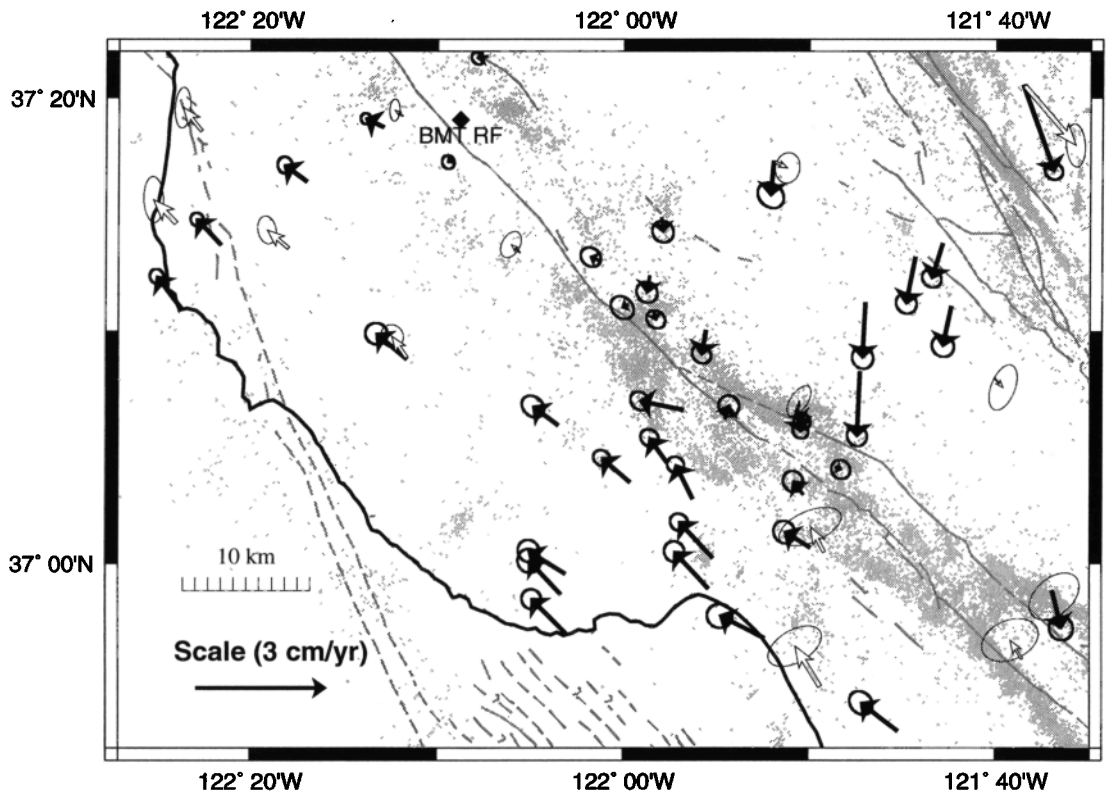

Figure 8. Close-up of postseismic (solid arrows relative to PAWT) and preseismic (open arrows relative to BMT RF located 2 km southeast of PAWT) velocities in the epicentral region of the Loma Prieta earthquake. The contraction northeast of the SAF observed in the postseismic data is not apparent in the preearthquake data.

east of the Calaveras fault appear to move toward the fault at an oblique angle. It is possible that this is the result of the complex series of creeping and locked fault segments along the Calaveras fault [*Oppenheimer et al.*, 1990]. Alternatively, the southern Calaveras or the southern Sargent faults may accommodate convergence by oblique slip [*Matsu'ura et al.*, 1986]. In any event, there is no postseismic data in the Hollister region, so this should not significantly affect our results. The model also underpredicts the velocities southwest of the SAF south of Loma Prieta by up to 3 mm/yr.

Postseismic Displacement Field Anomaly

Horizontal Displacements From GPS

The dislocation model of preseismic deformation can now be used to compute the predicted interseismic velocities and their uncertainties at all sites in the postseismic network. Subtracting the preearthquake velocities from the observed postseismic velocities yields the residual postseismic velocity field. The residual postseismic velocities shown in Figure 9 represent the component of the measured signal that exceeds the secular deformation field. The velocity field in Figure 9 is shown relative to PAWT, which we argue has not been affected by the Loma Prieta earthquake. VLBI measurements at Ford Ord (near BRUS) show that the velocity of BRUS relative to stable North America did not change significantly following the 1989 earthquake [*Bürgmann*, 1993; *Argus and Lyzenga*, 1994]. The insignificant change in the velocity of BRUS relative to PAWT suggests that the residual postseismic velocities are adequately tied to an external reference frame (Figure 9).

Along the Black Mountain profile, 44 km NW of the 1989 epicenter, postseismic velocities east of the Hayward fault agree well with their preearthquake estimates (Figure 9). ALLI appears to have an anomalous, southwesterly motion that is not observed at neighboring sites. The combined velocity determined for BAYS and Z137 is suspect owing to the problems associated with this site described above. Sites west of the SAF appear to have undergone a small but consistent acceleration, which is also observed at EAGL. Of the Loma Prieta profile sites east of the Calaveras fault, HAMI moved with a higher fault normal velocity following the earthquake. The two easternmost sites, MOCH and OSO1, have marginally significant westward directed motions.

The most significant residual postseismic motions occurred in a region around and northeast of Loma Prieta (Figure 9). Significant velocity increases and reorientations occurred in the near field of the earthquake. Fault-parallel velocities slightly increased by up to 8 mm/yr to the SW of the SAF. This acceleration is apparent at least as far to the NW as EAGL. The most surprising feature of the postseismic velocity field is a zone of SAF-normal contraction at rates exceeding 10 mm/yr, centered NE of Loma Prieta and extending as far east as HAMI across the Calaveras fault. The motion of AMER, located about midway between the two profiles, indicates that the zone of contraction extends beyond the NW end of the coseismic fault rupture. Unfortunately, we have little constraint on the extent of these motions southeast of the rupture zone.

Vertical Displacements From Leveling

The observed elevation changes are shown in Figure 6, together with a schematic cross section of active fault zones along the line [*McLaughlin*, 1990] and the first 2 years of aftershocks. The aftershocks shown in Figure 6 outline the dipping Loma Prieta rupture below 10 km, a vertical SAF above 10 km, and distributed seismicity NE of the SAF. Relative to Capitola, there is uplift of about 2 cm SW of the SAF, whereas the last 15 km of the line subsided by up to 3.5 cm. The steepest displacement gradient occurs directly in the hanging wall of the Berrocal fault zone (see also Figure 1). For comparison, the coseismic elevation changes on this line [*Marshall et al.*, 1991] are also shown in Figure 6. Notice that stations west of the Zayante fault, which uplifted coseismically owing to slip on the Loma Prieta fault, showed no vertical deformation between 1990 and 1992. The fact that the postseismic deformation is shorter wavelength than the coseismic uplift and the absence of deformation on the Santa Cruz coastal plain west of the Zayante fault, both indicate that the postseismic deformation is caused by shallow rather than deep sources. Note also that Loma Prieta, which subsided ~10 cm in the earthquake, uplifted ~1 cm postseismically.

The measured uplift exceeds by about an order of magnitude the average late Cenozoic uplift rate of the range [*Bürgmann et al.*, 1994]. Northeast of the SAF are a series of reverse structures dipping toward the SW that show evidence of Quaternary slip and whose late Cenozoic offsets produced much of the observed geologic uplift [*Bürgmann et al.*, 1994; *McLaughlin and Clark*, 1996]. Rapid geologic uplift of about 1 mm/yr can be deduced from apatite fission track ages, geomorphometric analyses, and offset Quaternary terraces and soil horizons [*Bürgmann et al.*, 1994; C.S. Hitchcock et al., unpublished data, 1994]. Uplift rates inferred from our model of preseismic deformation are also ≤1 mm/yr. We conclude that the uplift determined from leveling is likely to have been dominated by transient postseismic processes.

Data Interpretation and Models

In summary, the postseismic displacement field is characterized (1) by a ~40-km-wide zone of accelerated right-lateral shear, subparallel to the SAF, and centered near Loma Prieta and (2) by a zone of anomalous SAF-normal contraction across the foothills of the Santa Cruz Mountains and the adjacent Santa Clara valley, centered NE of Loma Prieta (Figure 9). The complex fault structure in the region does not allow an unambiguous identification of the source(s) of the postseismic deformation. We therefore evaluate a range of models based on the observed crustal deformation and additional geologic and geophysical evidence. We model the displacements with rectangular dislocations in an elastic half-space [e.g., *Okada*, 1985].

Previously Proposed Models

The postseismic displacement pattern following the Loma Prieta earthquake has also been interpreted by *Savage et al.* [1994] and by *Linker and Rice* [1996]. *Linker and Rice* [1996] model the displacement field resulting from the interaction of the earthquake rupture with a linear viscoelastic relaxation zone representing the deep aseismic portion of the fault. They also developed a nonlinear model with rate- and state-dependent friction on the downdip extension of the rupture. Their models, involving a relatively deep deformation source below the coseismic rupture, predict the fault-parallel velocities in the Loma Prieta profile quite well, but do not predict the observed fault-normal motions, and slightly overpredict the rates in the Black Mountain profile.

Savage et al. [1994] propose oblique slip on a 5-km-wide downdip extension of the Loma Prieta rupture plane (1.5 m right-lateral and 0.9 m reverse) and 0.1 m of fault-normal collapse from 5 to 16 km depth to explain the fault-normal motions observed along the Loma Prieta profile during the 3.3-year period of their observations. Adding a contractional dislocation to the model may represent gradual collapse by creep compaction of a dilatant fault zone created during the earthquake or may indicate leakage of pressurized pore water from the fault zone [*Savage et al.*, 1994]. *Savage et al.* [1994] also estimate right-lateral slip on vertical dislocations along the SAF (0.5 m) and the Calaveras fault (0.4 m) below 5 km that represent the background displacement field. That is, instead of subtracting the preseismic displacement field from the postseismic measurements, they solve for the postseismic anomaly and the secular displacement rates. This model predicts the horizontal displacement measurements quite well but significantly misfits the leveling data, as shown below.

Previously, we proposed a model involving postseismic slip on 2 faults that fits the first 2 years of GPS data [*Bürgmann and Segall*, 1991; *Bürgmann et al.*, 1996]. The best fit model for the early GPS data included predominantly strike slip on the Loma Prieta coseismic rupture and reverse slip on a shallow, southwest dipping fault northeast of the SAF [*Bürgmann et al.*, 1996]. Here we evaluate models based on the leveling data and 4.5 years of GPS data.

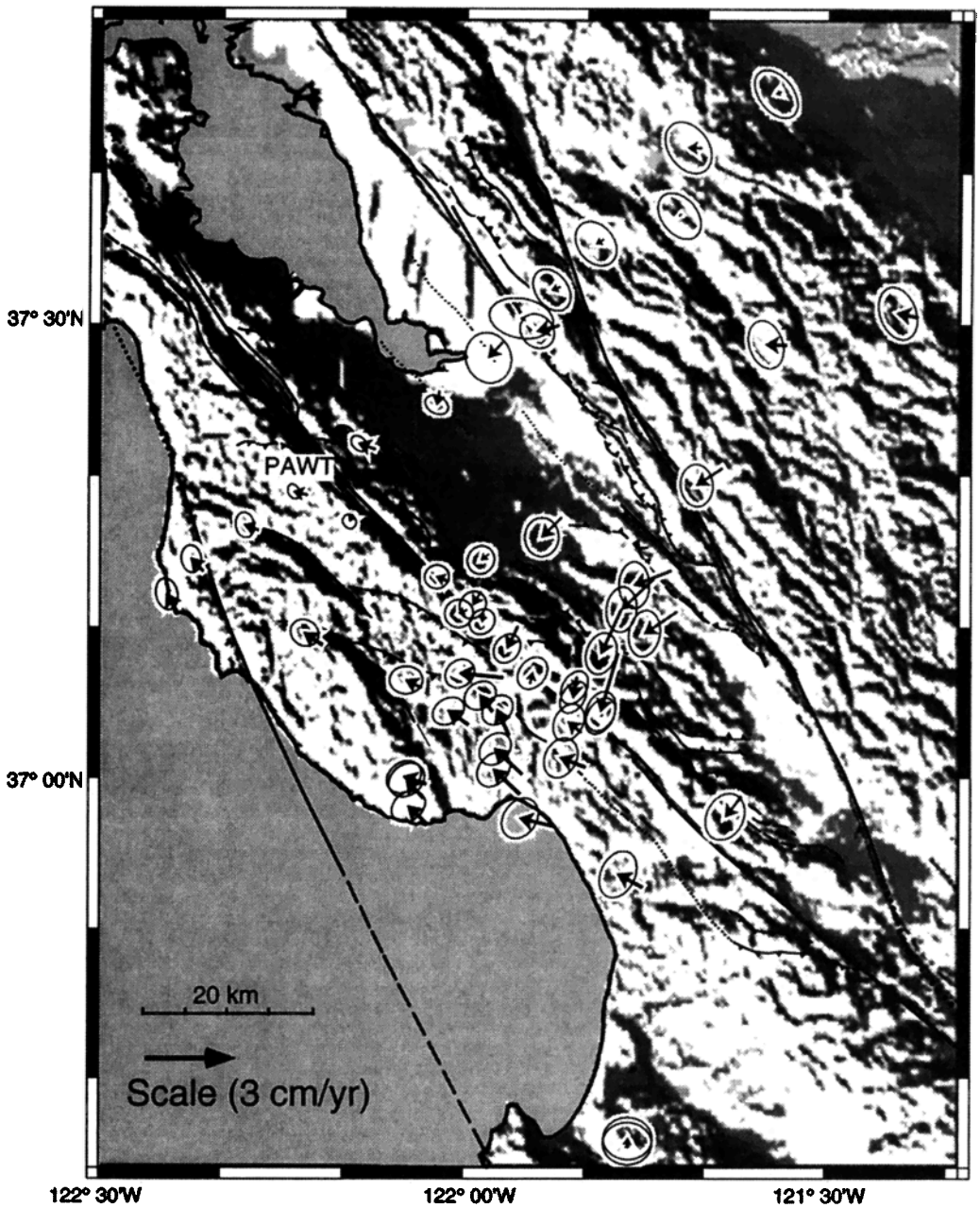

Figure 9. Residual velocities determined by subtracting the preearthquake model velocities from our observations. Note a slight acceleration of fault-parallel motions SW of the SAF and pronounced contraction NE of the SAF.

First-Order Models

We first develop a series of first-order models to illustrate the characteristic displacement fields for a number of possible sources. We then test previously proposed models of postseismic relaxation and develop a model that best satisfies geologic and geophysical constraints (Table 5).

Previously observed or predicted postseismic relaxation processes include accelerated shear below the coseismic rupture and aseismic slip within or adjacent to the rupture zone (Figure 10). Oblique slip on a 5-km-wide, SW dipping fault below the hypocenter (16.8 km) with equal amounts of strike slip and dip slip (as in the mainshock) produces westerly oriented displacements and broadly distributed uplift SW of the fault and southerly motions to the NE of the fault (Figure 10a). The zone of anomalous deformation is approximately 60 km wide. Oblique slip on the coseismic rupture from 8 to 16.8 km depth produces a similar displacement field but with larger displacements spread over a narrower region (Figure 10b). Figure 10c evaluates the effect of fault zone collapse. This model predicts an asymmetric zone of contraction, as well as significant subsidence SW of the fault and a small amount of uplift NE of the fault. A model of reverse slip on a shallow, 45° SW dipping fault from 3.5 to 8 km depth produces a ~40-km-wide zone of contraction and a narrow uplift zone centered above the thrust (Figure 10d). None of these simple models predicts the observed pattern of the horizontal and vertical motions.

Kinematic Models From Nonlinear Inversions

We continue our analysis by formally inverting for model fault parameters. We use a constrained, nonlinear optimization algorithm described by *Arnadottir and Segall* [1994], which allows us to estimate the geometry (parameterized by length, depth, width, dip, strike, and location) and the rates of strike slip, dip slip, and opening of one or more faults that best fit the GPS and leveling data. Specifically, we seek models that minimize the weighted residual sum of squares (WRSS) (Table 5). It is possible to apply bounds (such as constraints on the depth of faulting or range of permissible fault strikes) to find best fitting sources representing, for example, deep shear or slip on the coseismic rupture. Table 5 summarizes the results from a series of models. For comparison, note that a null model with no postseismic deformation has a model misfit $\sqrt{\mathrm{WRSS}/(n-p)} = 3.26$ (Table 5).

To test the possibility of postseismic slip downdip of the earthquake, we constrain the strike (132°) and dip (70°) to be the same as the coseismic rupture and force the depth to be greater than the mainshock hypocentral depth (16.8 km). Note that if we loosen the depth constraint, the inversion favors shallower model faults. The model misfit $\sqrt{\mathrm{WRSS}/(n-p)} = 3.12$ indicates that models of postseismic relaxation below the earthquake rupture fit the data very poorly. In particular, the deep source fails to reproduce the fault-normal displacements and produces a poorer fit to the leveling data than the null model. The deep-slip model (see Figure 10a) predicts westerly directed motions SW of the SAF rather than the observed fault-parallel motions. It also predicts a region of broad uplift SW of the fault and a very gentle gradient NE of Loma Prieta, both features not observed in the data.

Next, we evaluate models of continued slip on the coseismic rupture dipping 70° and striking 132° [*Lisowski et al.*, 1990a]. The best fitting model fault in this class lies close to the Loma Prieta rupture and has the maximum permitted fault width (from

Table 5. Fault Parameters for Geodetically Determined Models From Nonlinear Inversion of GPS and Leveling Data

Model	Length Along Strike, km	Depth to Bottom, km	Width Along Dip, km	Dip, °SW	Azimuth, deg	Latitude, deg	Longitude, deg	Dip Slip, m/yr	Standard Deviation	Strike Slip, m/yr	Standard Deviation	Opening, m/yr	Standard Deviation	WRSS	WRSS, GPS	WRSS, Level	Misfit
Null model								0.000	0.000	0.000	0.000	0.000	0.000	2241	1761	480	3.26
							One-Fault Models										
Downdip of "LP fault"	53.96	17.82	(3.00)	[70]	[132]	(37.03)	-(121.90)	0.107	0.012	-0.211	0.024	none		2030	1531	499	3.12
"Loma Prieta fault"	(45.00)	(16.80)	(12.55)	[70]	[132]	(37.00)	-121.83	0.008	0.002	-0.047	0.003	none		1970	1510	460	3.07
"Unconstrained"	92.24	90.29	(150.00)	36	132.90	36.13	-122.60	0.017	0.001	-0.013	0.001			1537	1057	480	2.71
							Collapse Models										
"Loma Prieta fault" with fault zone collapse	38.03	(16.80)	(12.55)	[70]	[132]	(37.00)	-121.83	0.018	0.002	-0.048	0.003	-0.027	0.001	1595	1157	438	2.77
LP collapse	28.14	14.44	10.04	[70]	[132]	(37.02)	-(121.86)	none		none		-0.035	0.002	1517	1079	438	2.70
with creep below	47.39	(20.69)	(5.10)	[70]	[132]	(37.01)	-(121.88)	0.137	0.010	-0.134	0.020	none					
							Two-Fault Model										
"Loma Prieta fault"	53.82	15.57	(15.00)	70	(130.00)	36.96	-121.78	0.017	0.001	-0.018	0.001	none		1310	966	343	2.52
Shallow thrust	61.40	6.11	8.99	(30)	(132)	37.04	-121.85	0.025	0.001	0.002	0.001	none					

WRSS is weighted residual sum of squares. Latitude and longitude refer to the center of bottom fault edge. Model misfit is $\sqrt{\mathrm{WRSS}/(n-p)}$, where n is the number of data and p is the number of model parameters. Numbers in parentheses reached bounding constraint. Numbers in brackets denote tightly constrained.

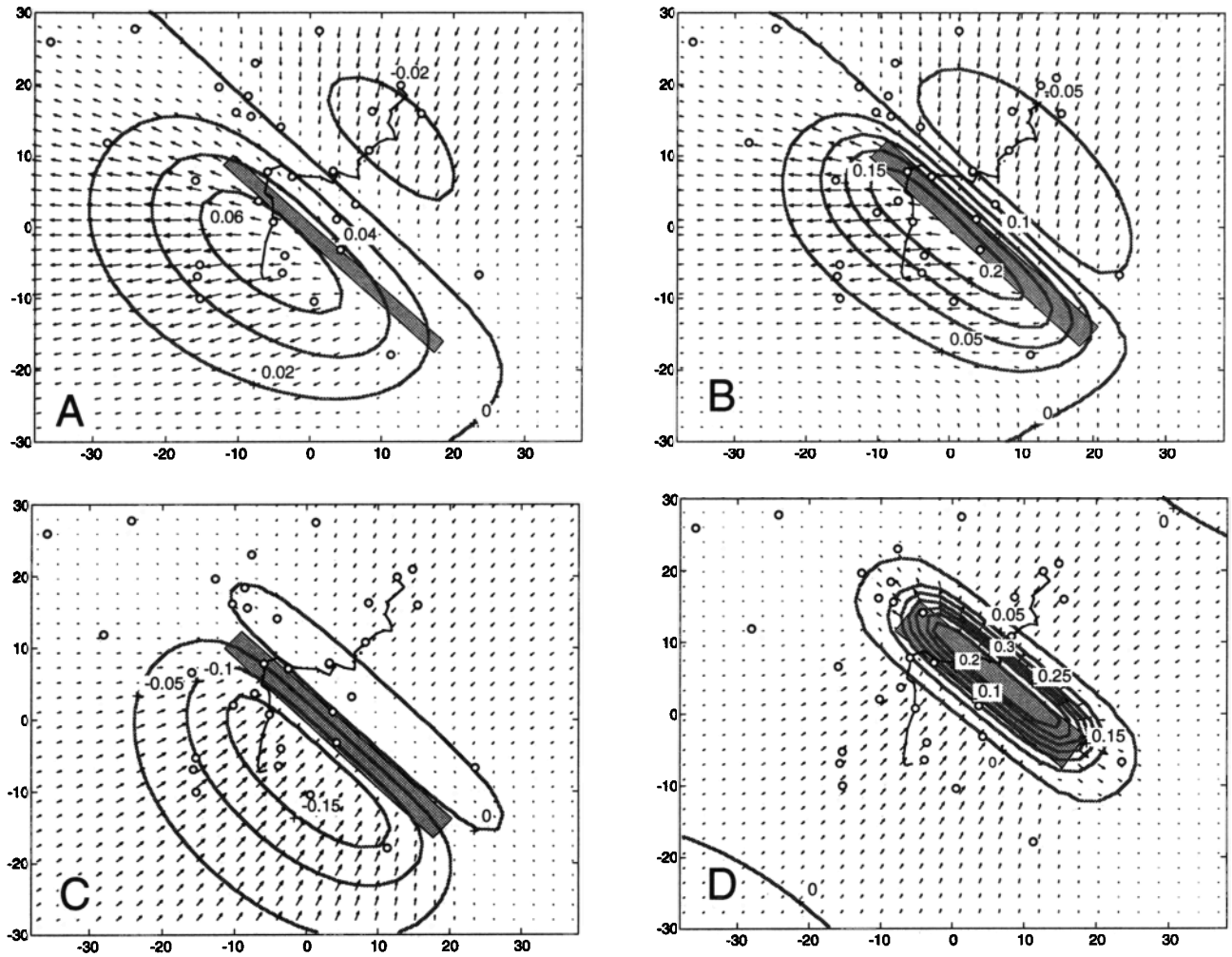

Figure 10. Displacement fields computed from first-order models of proposed sources of postseismic deformation. The locations of GPS stations (circles) and the leveling line (solid line) and the shaded surface projections of the model faults are shown. (a) Oblique slip below the Loma Prieta hypocenter (16.8 to 21.5 km depth on 70°SW dipping fault). Unit slip produces up to 0.07 units of uplift SW of the fault. (b) Oblique slip on coseismic rupture (8 to 16.8 km depth on 70°SW dipping fault). (c) Collapse of coseismic rupture. (d) Reverse slip on shallow thrust fault (3.5 to 8 km depth on 45°SW dipping fault).

16.8 to 5 km depth) and maximum length of 45 km. The slip is nearly pure strike slip at a rate of ~5 cm/yr. If we remove the depth constraint on the upper edge of the dislocation, the best fitting model fault extends to 1 km depth and the misfit is reduced to 2.97 (not shown in Table 5). As seen in Figure 10b, models with slip in the coseismic rupture zone also fail to predict the general characteristics of the observed deformation. The best fitting, unconstrained single fault is implausibly deep and is not judged to be geologically reasonable (Table 5).

Savage et al. [1994] suggested that fault zone compaction, together with accelerated fault creep below the coseismic rupture, may explain the observed motions. The displacement field from a collapse model shown in Figure 10c indicates asymmetric contraction and subsidence to the SW of the SAF. Adding these displacements to those in Figure 10a results in horizontal displacements that resemble those we observe. We test two models that include fault zone collapse. A model that involves slip, as well as contraction across the coseismic rupture with the same dip, strike, and depth constraints as the previous rupture model, produces an improved fit to the GPS data but does not fit the leveling data well. A model resembling *Savage et al.*'s [1994] favored model of fault collapse and creep below the rupture plane fits the GPS data even better, but it does not improve the fit of the leveling data (Figure 11). The favored rate of fault zone collapse is 3.5 cm/yr, for a total of about 15 cm during the ~4-year observation period, on a 10-km-wide and 28-km-long model fault. About 20 cm/yr of oblique slip on a 5-km-wide downdip extension of the coseismic rupture is also predicted.

Because of the known thrust faults in the Santa Cruz Mountains, the observed coseismic ground deformation along these faults, and the predominance of reverse mechanisms of aftershocks NE of the SAF, we have previously suggested that the observed contraction is due to reverse faulting [*Bürgmann et al.*, 1996]. Slip on a shallow thrust fault produces localized uplift and contraction across the fault (Figure 10d). Clearly, shallow thrust faulting alone cannot predict the observed motions. We find that a two-fault model is required to fit the observed horizontal and vertical velocities.

A model that includes slip on two faults, reverse and strike-slip on a fault near the SAF zone and thrusting on a fault NE of the SAF, provides the best fit to the GPS and leveling data

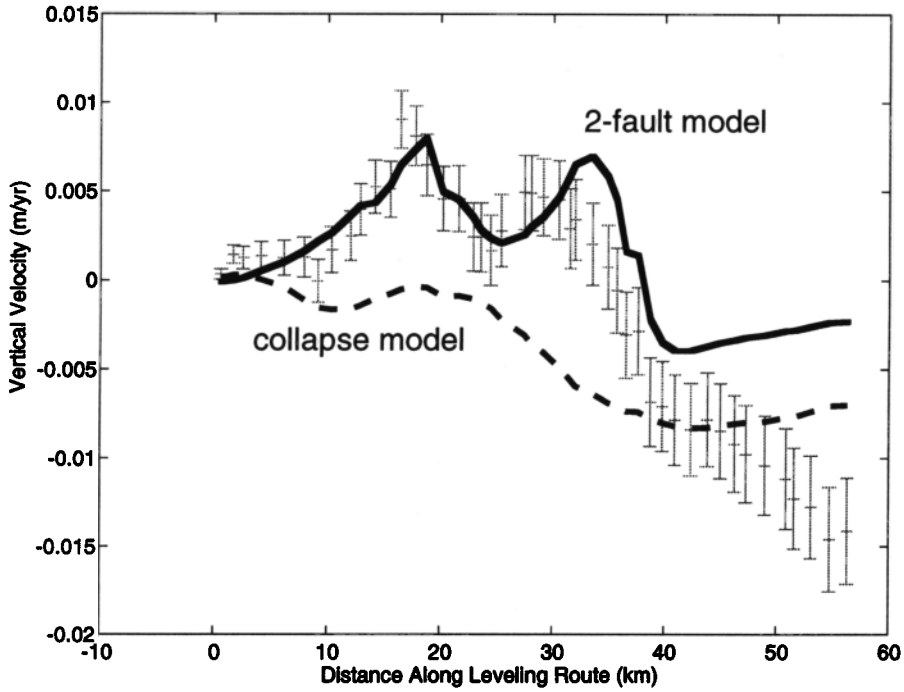

Figure 11. Measured vertical velocities (with error bars) and vertical velocities predicted from the two-fault model (solid line) shown in Figure 12. The model predicts the overall pattern of uplift but does not predict the continued drop off at the NE end of the leveling line. Also shown (dashed line) are the predicted velocities from a model involving collapse of the Loma Prieta rupture and oblique slip below.

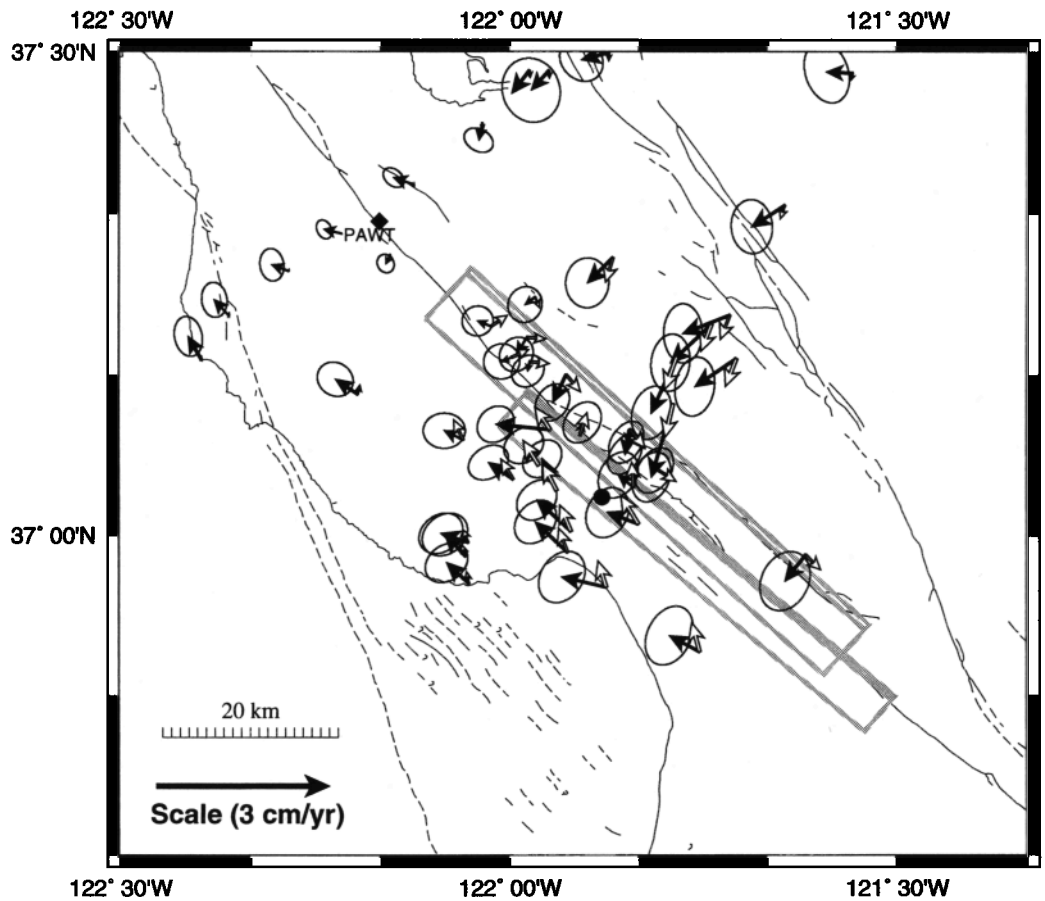

Figure 12. Postseismic residual velocities (solid arrows with 95% confidence ellipses) and velocities computed from the best fitting dislocation model involving slip on two faults (open arrows). The two rectangles show the projections of the faults used to compute the modeled station velocities (See Table 5 for model parameters).

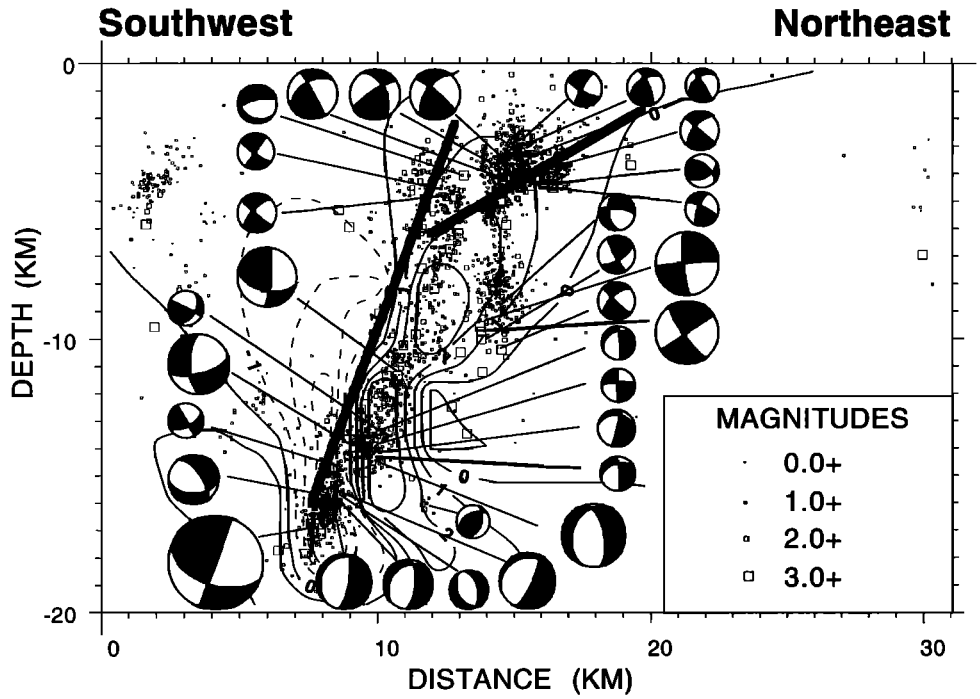

Figure 13. Contoured stress changes (in megapascals) induced by the Loma Prieta earthquake on 45° SW dipping fault planes. The coseismic displacement distribution determined by *Beroza* [1991] is discretized into 272 uniform slip fault elements in an elastic, isotropic, and homogeneous half-space. Both fault-normal stresses and dip-parallel shear stresses influence the faults through a Coulomb failure criterion with a coefficient of friction $\mu = 0.6$. Also shown are the two model faults from Figure 11 (solid lines). The first fault lies a few kilometers above the Loma Prieta rupture; the second fault lies in a cluster of seismicity NE of the SAF. Focal mechanisms of the main shock and 1989-1994 aftershocks ($M \geq 2.5$; projected onto a vertical N40°E striking plane) from a ~10-km-wide profile across the SAF show a predominance of thrust mechanisms NE of the fault. The focal mechanisms are from the Northern California Earthquake Data Center selected using standard quality criteria [*Oppenheimer et al.*, 1990].

(Table 5 and Figures 11 and 12). One model fault dips at a comparable angle to the "Loma Prieta fault" and has subequal thrust and strike-slip components, but it is shallower than the coseismic rupture (Figure 13). The second model fault, located NE of the SAF, is quite long, dips at the lower bound (30°) of permitted fault dips, and accommodates 2.4 cm/yr of thrust faulting. The SE ends of the model faults are not well constrained by the network and extend farther than the coseismic Loma Prieta rupture.

We find that this model predicts all the first-order patterns observed in the postseismic data, including accelerated fault parallel motion SW of the SAF, as well as contraction and associated uplift NE of the fault (Figure 11). This model fits the horizontal data well but underpredicts somewhat the fault-normal motions in the eastern Santa Clara Valley and at Mount Hamilton (Figure 12). It also slightly underpredicts the fault-parallel velocities SW of the SAF. Figure 11 shows the observed and predicted vertical velocities along the leveling line for the best fitting two-fault model. The model fits the data well from the Pacific coast to the western edge of Santa Clara Valley. However, it does not predict the continued subsidence pattern at the NE end of the leveling line.

Although this is the best fitting, most geologically reasonable model we have found, the misfit of 2.5 indicates that the model does not fully explain the data within the reported errors. This may be caused by an underestimate of the errors in the data or in the computed interseismic correction. Alternatively, the misfit may indicate that our model insufficiently represents the physical processes and fault geometries responsible for the deformation. Material heterogeneities, multiple fault surfaces, complex slip distributions, and distributed inelastic deformation may contribute to the misfit.

Discussion of Model Results

We find that single-source models do not adequately explain the observed postseismic deformations. Accelerated flow or fault slip below the coseismic rupture does not appear to be the main source of the observed deformation. Deep processes produce long-wavelength displacement fields, not the narrowly focused deformation we observe. We find that much of the deformation is best explained by relatively shallow sources above 15 km depth. Our preferred model involves contemporaneous oblique slip and thrust faulting at high rates on two faults with similar strikes. The dip of the first fault is not tightly constrained and we cannot clearly differentiate if slip occurs on the SAF or the Loma Prieta rupture. However, we find that fault slip extends to very shallow depths, suggesting that faulting took place updip of the Loma Prieta fault. The inferred slip on the SAF or Loma Prieta fault may represent creep above or between the two high-slip asperities that released most of the earthquake moment [*Beroza*, 1991; *Hartzell et al.*, 1991; *Wald et al.*, 1991; *Arnadottir and Segall*, 1994; *Horton*, 1996].

The Foothills thrust belt has been active in the Quaternary and experienced shallow, triggered slip during the Loma Prieta earthquake [*Haugerud and Ellen*, 1990; *McLaughlin*, 1990]. Our model thrust fault appears to coincide with the Berrocal fault zone, but it is possible that postseismic slip is distributed among several faults in this complex thrust system. Focal mechanisms of $M \geq 2.5$ Loma Prieta aftershocks, located NE of the SAF near the Berrocal fault zone, indicate that these events occurred predominantly on reverse faults (Figure 13). The seismicity near the Loma Prieta rupture, on the other hand, is very complex, with all types of fault plane solutions [*Oppenheimer*, 1990; *Beroza and Zoback*, 1993]. Note that the fault slip we model exceeds by several orders of magnitude the slip accumulated in aftershocks and must be dominantly aseismic.

Discussion

Stress redistribution accompanying the Loma Prieta mainshock would increase the loading on thrust faults NE and updip of the rupture [*Reasenberg and Simpson*, 1992]. Figure 13 shows a cross section perpendicular to the SAF with the contoured coseismic stress changes on thrust faults NE of the SAF overlaid on a plot of the aftershocks and the model faults. Shear stress changes and the thrust-normal stress changes both affect the loading of N60°W striking, 45° dipping thrust planes through a Coulomb failure function [*Reasenberg and Simpson*, 1992] $CFF = \tau_S + \mu\sigma_n$, where τ_S is the shear traction in the dip direction, σ_n is the fault-normal traction, and μ is the coefficient of friction. A coefficient of friction of 0.6 has been chosen for the model in Figure 13. As the complex slip distribution during the earthquake is expected to be important in the induced stress field in the close vicinity of the earthquake rupture, we used the heterogeneous fault slip model of Beroza [1991] to compute the stress changes. Coseismically induced stress changes of 1 to 2 MPa that enhance thrust loading occurred NE of the SAF. The stress changes on fault planes of somewhat different strikes and dips are comparable to those shown. Apparently, the increased microseismicity and the aseismic thrusting inferred from geodetic data reflect deformation in response to the load increase.

An enigma associated with the Loma Prieta earthquake was the observation that the highest topography of the Santa Cruz Mountains around Loma Prieta subsided by ~10 cm during the earthquake [*Lisowski et al.*, 1990a]. Long-term uplift rates in the Loma Prieta area deduced from apatite fission track dating and geomorphic analyses average about 1 mm/yr over the last 5 m.y. [*Bürgmann et al.*, 1994]. While different fault plane geometries could produce the long-term uplift pattern [*Schwartz et al.*, 1990], slip on the reverse faults at the base of the southern Santa Cruz Mountains at combined rates of 2-3 mm/yr would result in the topographic expression of the southern Santa Cruz Mountains [*Bürgmann et al.*, 1994]. Our measurements indicate that some of this uplift may occur concurrently with aseismic fault slip at depth on the Berrocal fault zone following large regional earthquakes.

Accelerated slip on faults in the San Francisco Bay region will change the loading of nearby segments of the SAF and the Hayward fault. A detailed analysis of coseismic static stress changes on bay area faults shows that microseismicity rates increased or decreased in accordance with the computed stresses [*Reasenberg and Simpson*, 1992]. Reduced creep rates, observed along the southern Hayward and Calaveras faults following the earthquake, are evidence of induced left-lateral shear stress across these faults [*Galehouse*, 1992; *Lienkaemper et al.*, 1992]. *Bürgmann et al.* [1996] modeled the change in loading on NW striking fault planes due to the Loma Prieta earthquake and postseismic fault slip with the method outlined above, assuming that fault-parallel shear stress, as well as fault normal stresses, determine the fault response through a Coulomb failure criterion. Postseismic fault slip further increases the load on the SAF immediately to the NW of the Loma Prieta rupture, while both the coseismic and the postseismic static stress changes have a retarding effect on the Hayward fault zone and most of the Calaveras and San Gregorio-Hosgri fault zones. The yearly postseismic stress changes are about an order of magnitude less than those induced coseismically.

Similar postseismic adjustments occurred following the 1979 Coyote Lake and the 1984 Morgan Hill earthquakes along the Calaveras fault [*Oppenheimer et al.*, 1990]. While the coseismic stress perturbations on neighboring fault segments induced by these moderate earthquakes were negligible [*Du and Aydin*, 1993], postseismic fault creep adjacent to the coseismic ruptures may have caused the observed south-to-north propagation of earthquakes along the Calaveras fault [*Oppenheimer et al.*, 1990].

The stress changes caused by coseismic and postseismic fault slip only add to those accumulated by background loading of the bay area faults. The January 15, 1993, Gilroy earthquake that occurred in a region of induced left-lateral shear, east of the southern termination of the Loma Prieta rupture is a timely reminder of this. The peninsular segment of the SAF, the updip extension of the Loma Prieta rupture (from about 8 km to the surface), and several thrust faults that parallel the SAF through most of the bay region appear to represent significant seismic hazards since the Loma Prieta earthquake. Continued reverse faulting may also relieve normal traction along the southern Hayward fault and increase the likelihood of faulting there, despite a decrease in right-lateral stress.

In 1865 a M ~6.5 earthquake occurred in the southern Santa Cruz Mountains [*Ellsworth*, 1990]. *Tuttle and Sykes* [1992] noted that intensities for this event were greater in San Jose in comparison to the Loma Prieta earthquake but were less in Monterey. On this basis, *Tuttle and Sykes* [1992] suggested that the 1865 event was located NE of the SAF. In their reanalysis of 19th century triangulation data in the San Francisco Bay area, *Yu and Segall* [1996] found that station Loma Prieta was displaced NE, perpendicular to the strike of the SAF, between 1850 and 1880, presumably as a result of the 1865 earthquake. The observed fault-normal displacement is inconsistent with slip on the Loma Prieta rupture and not easily explained by slip on the SAF. The fault-normal displacement is, however, exactly what would be expected for slip on a southwest dipping thrust fault located NE of the SAF. Slip on the shallow dipping thrust fault shown in Figures 12 and 13, with moment equivalent to a M 6 3/4 quake, explains the 1850-1880 displacements quite well [*Yu and Segall*, 1996]. Taken together, these observations suggest, but certainly do not prove, that the 1865 earthquake was caused by slip on a thrust fault in the Foothills thrust belt and that the same fault(s) slipped aseismically following the Loma Prieta earthquake. We note that an earthquake comparable to the 1865 event would constitute a significant hazard to the south San Francisco Bay region.

Conclusions

Leveling and GPS data collected during 5 years following the 1989 Loma Prieta earthquake show a significant acceleration of deformation within about 20 km of the Loma Prieta rupture. The most striking feature in the postseismic motions is a zone of rapid uplift and contraction northeast of the SAF. Model inversions of the postseismic data suggest that aseismic oblique-reverse slip on the SAF and/or the Loma Prieta rupture and thrusting along the Foothills thrust belt are the most likely sources of the observed deformation. The first few years of postseismic deformation are dominated by aseismic fault slip updip of the coseismic rupture, probably triggered by coseismic stress changes. We do not find conclusive evidence for accelerated shear below the rupture or fault zone collapse. Continued monitoring of the transient deformation will provide valuable information about mechanisms of time-dependent deformation following a large earthquake and its effects on neighboring faults.

Acknowledgments. We thank a large number of students, faculty, and friends at Stanford University, U.C. Santa Cruz, and U.C. Davis, who helped collect GPS data along the Black Mountain profile and the Santa Cruz Mountain network during the last 5 years. We also acknowledge the efforts of the U.S. Geological Survey crustal deformation field crew in collecting invaluable GPS data starting just 2 days after the Loma Prieta earthquake. The leveling data were collected by the National Geodetic Survey field crew. Grant Marshall gave invaluable advice on analyzing the leveling data. We thank Thora Arnadottir, Jeff Freymueller, Kristine Larson, and Mark Murray for providing programs and much advice for the GPS data analysis and modeling. Richard Snay and an anonymous reviewer provided helpful comments. This research was supported, in part, by NSF grants EAR-9003575, EAR-9002164, and EAR-9116117 and U.S. Geological Survey award 1434-94-G-2447 to Stanford University and 1434-HG-96-GR-02744 to U.C. Davis.

References

Anderson, D.L., Accelerated plate tectonics, *Science, 187*, 1077-1079, 1975.

Argus, D.F., and G.A. Lyzenga, Site velocities before and after the Loma Prieta and Gulf of Alaska earthquakes determined from VLBI, *Geophys Res Lett, 21*, 333-336, 1994.

Arnadottir, T., and P. Segall, The 1989 Loma Prieta earthquake imaged from inversion of geodetic data, *J. Geophys. Res., 99*, 21,835-21,855, 1994.

Aydin, A., and B.M. Page, Diverse Pliocene-Quaternary tectonics in a transform environment, San Francisco Bay region, California, *Geol. Soc. Am. Bull., 95*, 1303-1317, 1984.

Aydin, A., A.M. Johnson, and R.W. Fleming, Right-lateral-reverse surface rupture along the San Andreas and Sargent faults associated with the October 17, 1989, Loma Prieta, California, earthquake, *Geology, 20*, 1063-1067, 1992.

Behr, J., R. Bilham, P. Bodin, R.O. Burford, and R. Bürgmann, Aseismic slip on the San Andreas fault south of Loma Prieta, *Geophys. Res. Lett., 17*, 1445-1448, 1990.

Behr, J., R. Bilham, and P. Bodin, Increased surface creep rates on the San Andreas fault southeast of the Loma Prieta mainshock, *U.S. Geol. Surv. Prof. Pap., 1550*, in press, 1996.

Beroza, G.C., Near-source modeling of the Loma Prieta earthquake: Evidence for heterogeneous slip and implications for earthquake hazard, *Bull. Seismol. Soc. Am., 81*, 1603-1621, 1991.

Beroza, G.D., and M.D. Zoback, Mechanism diversity of the Loma Prieta aftershocks and the mechanics of mainshock-aftershock interaction, *Science, 259*, 210-213, 1993.

Beutler, G., I. Bauersima, W. Gurtner, M. Rothacher, T. Schildknecht, G.L. Mader, and M.D. Abell, Evaluation of the 1984 Alaska Global Positioning System campaign with the Bernese GPS software, *J. Geophys. Res., 92*, 1295-1303, 1987.

Bilham, R., Surface slip subsequent to the 24 November 1987 Superstition Hills, California, earthquake monitored by digital creepmeters, *Bull. Seismol. Soc. Am., 79*, 424-450, 1989.

Bott, N.H.P., and D.S. Dean, Stress diffusion from plate boundaries, *Nature, 243*, 339-341, 1973.

Budianski, B., and C. Amazigo, Interaction of fault slip and lithosphere creep, *J. Geophys. Res., 81*, 4897-4900, 1976.

Bürgmann, R., Deformation associated with strike-slip faults, Ph.D. thesis, 186 pp; Stanford Univ., Stanford, Calif., 1993.

Bürgmann, R., and P. Segall, Postseismic GPS monitoring NW of the 1989 Loma Prieta rupture zone(abstract), Eos Trans. AGU, *72*(44), Fall Meet. Suppl., 119, 1991.

Bürgmann, R., P. Segall, M. Lisowski, G. Marshall, R. Stein, and J.P. Svarc, Post-seismic uplift of the southern Santa Cruz Mountains following the Loma Prieta earthquake, *Eos Trans. AGU, 74*(16), Spring Meet. Suppl., 106, 1993.

Bürgmann, R., R. Arrowsmith, T. Dumitru, and R. McLaughlin, Rise and fall of the southern Santa Cruz Mountains, California, deduced from fission track dating, geomorphic analysis, and geodetic data, *J. Geophys. Res., 99*, 20,181-20,202, 1994.

Bürgmann, R., P. Segall, M. Lisowski, and J.L. Svarc, Decay of postseismic strain anomaly following the 1989 Loma Prieta, California, earthquake, paper presented at XXI General Assembly, Int. Union of Geod. and Geophys., Boulder, Colorado, 1995.

Bürgmann, R., P. Segall, M. Lisowski, and J.P. Svarc, Post-seismic strain following the 1989 Loma Prieta earthquake from repeated GPS measurements, *U.S. Geol. Surv. Prof. Pap., 1550*, in press, 1996.

Cohen, S.C., Postseismic surface deformations due to lithospheric and asthenospheric viscoelasticity, *Geophys. Res. Lett., 6*, 129-131, 1979.

Davis, J.L., W.H. Prescott, J.L. Svarc, and K.J. Wendt, Assesment of Global Positioning System measurements for studies of crustal deformation, *J. Geophys. Res., 94*, 13,635-13,650, 1989.

Dietz, L.D., and W.L. Ellsworth, The October 17, 1989, Loma Prieta, California, earthquake and its aftershocks: Geometry of the sequence from high-resolution locations, *Geophys. Res. Lett., 17*, 1417-1420, 1990.

Du, Y., and A. Aydin, Stress transfer during three sequential moderate earthquakes along the central Calaveras fault, California, *J. Geophys. Res., 98*, 9947-9962, 1993.

Du, Y., A. Aydin, and P. Segall, Comparison of various inversion techniques as applied to the determination of a geophysical deformation model for the 1983 Borah Peak earthquake, *Bull. Seismol. Soc. Am., 82*, 1840-1866, 1992.

Ellsworth, W.L., Earthquake history, 1769-1989, in *The San Andreas Fault System, Calfornia*, edited by R.E. Wallace, *U.S. Geol. Surv. Prof. Pap.*, 153-181, 1990.

Galehouse, J.S., Creep rates and creep characteristics of eastern San Francisco Bay area faults:1979-1992, Spec. Publ. *Calif. Div. Mines Geol., 113*, 45-53, 1992.

Gwyther, R.L., M.T. Gladwin, and R.H.G. Hart, A shear strain anomaly following the Loma Prieta earthquake, *Nature, 356*, 142-144, 1992.

Hartzell, S.H., G.S. Stewart, and C. Mendoza, Comparison of L_1 and L_2 norms in a teleseismic waveform inversion for the slip history of the Loma Prieta, California, earthquake, *Bull. Seismol. Soc. Am., 81*, 1518-1539, 1991.

Haugerud, R.A., and S.D. Ellen, Coseismic ground deformation along the northeast margin of the Santa Cruz Mountains, in *Field Guide to Neotectonics of the San Andreas Fault System, Santa Cruz Mountains, in Light of the Loma Prieta Earthquake*, edited by D.P. Schwartz and D.J. Ponti, U.S. Geol. Surv., Open File Rep., 32-37, 1990.

Horton, S., A fault model with variable slip duration for the 1989 Loma Prieta, California, earthquake determined from strong-ground-motion data, *Bull. Seismol. Soc. Am., 86*, 122-132, 1996.

Kasahara, K., *Earthquake Mechanics*, 248 pp., Cambridge Univ. Press, New York, 1981.

King, G.C.P., A.G. Lindh, and D.H. Oppenheimer, Seismic slip, segmentation, and the Loma Prieta earthquake, *Geophys. Res. Lett., 17*, 1449-1452, 1990.

Kouba, J., Analysis coordinator report, in *International GPS Service for Geodynamics 1994 Annual Report*, edited by J. F. Zumberge, and R E Neilan, 1995.

Langbein, J.O., Post-seismic slip on the San Andreas fault at the northwestern end of the 1989 Loma Prieta earthquake rupture zone, *Geophys. Res. Lett., 17*, 1223-1226, 1990.

Larson, K.M., F.H. Webb, and D.C. Agnew, Application of the Global Postioning System to crustal deformation measurements, 2, The influence of errors in orbit determination networks, *J. Geophys. Res., 96*, 16,567-16,584, 1991.

Lehner, F.K., V.C. Li, and J.R. Rice, Stress diffusion along rupturing plate boundaries, *J. Geophys. Res., 86*, 6155-6169, 1981.

Li, V.C., and J.R. Rice, Crustal deformation in great California earthquake cycles, *J.Geophys.Res.*, *92*, 11,533-11,551, 1987.

Lienkaemper, J.J., J.S. Galehouse, and R.W. Simpson, Hayward fault, California: Longterm creep rates versus slower creep since 1989 Loma Prieta earthquake(abstract), Eos Trans. AGU, *73*(43), Fall Meet. Suppl. 119, 1992.

Linker, M.F., and J.R. Rice, Models of postseismic deformation and stress transfer associated with the 1989 Loma Prieta earthquake, *U.S. Geol. Surv. Prof. Pap.*, *1550*, in press, 1996.

Lisowski, M., W.H. Prescott, J.C. Savage, and M.J. Johnston, Geodetic estimate of coseismic slip during the 1989 Loma Prieta, California earthquake, *Geophys. Res. Lett.*, *17*, 1437-1440, 1990a.

Lisowski, M., W.H. Prescott, J.C. Savage, and J.L. Svarc, A possible geodetic anomaly observed prior to the Loma Prieta, California, earthquake, *Geophys. Res. Lett.*, *17*, 1211-1214, 1990b.

Lisowski, M., J.C. Savage, and W.H. Prescott, The velocity field along the San Andreas fault in central and southern California, *J. Geophys. Res.*, *96*, 8369-8389, 1991.

Marshall, G.A., R.S. Stein, and W. Thatcher, Faulting geometry and slip from co-seismic elevation changes: The October 17, 1989 Loma Prieta, California, earthquake, *Bull. Seismol. Soc. Am.*, *81*, 1660-1693, 1991.

Matsu'ura, M., D.D. Jackson, and A. Cheng, Dislocation model for aseismic crustal deformation at Hollister, California, *J. Geophys. Res.*, *91*, 12,661-12,674, 1986.

McLaughlin, R., Stop 4. Sargent fault zone at Loma Prieta, in *Field Guide to Neotectonics of the San Andreas Fault System, Santa Cruz Mountains, in Light of the Loma Prieta Earthquake*, edited by D.P. Schwartz and D.J. Ponti, U.S. Geol. Surv., Open File Rep. 19-22, 1990.

McLaughlin, R.J., and E.E. Clark, Stratigraphy and structure of rocks across the San Andreas fault zone near Loma Prieta, California: Their relation to deformation during the October 17, 1989 earthquake, *U.S. Geol. Surv. Prof. Pap.*, *1550*, in press, 1996.

Nur, A., and G. Mavko, Postseismic viscoelastic rebound, *Science*, *183*, 204-206, 1974.

Okada, Y., Surface deformation due to shear and tensile faults in a half-space, *Bull. Seismol. Soc. Am.*, *75*, 1135-1154, 1985.

Oppenheimer, D.H., Aftershock slip behavior of the 1989 Loma Prieta, California earthquake, *Geophys. Res. Lett.*, *17*, 1199-1202, 1990.

Oppenheimer, D.H., W.H. Bakun, and A.G. Lindh, Slip partitioning of the Calaveras fault, California, and prospects for future earthquakes, *J. Geophys. Res.*, *95*, 8483-8498, 1990.

Pollitz, F.F., Postseismic relaxation theory on the spherical earth, *Bull. Seismol. Soc. Am.*, *82*, 422-453, 1992.

Pollitz, F.F., and I.S. Sacks, Modeling of postseismic relaxation following the great 1857 earthquake, southern California, *Bull. Seismol. Soc. Am.*, *82*, 454-480, 1992.

Reasenberg, P.A., and R.W. Simpson, Response of regional seismicity to the static stress change produced by the Loma Prieta earthquake, *Science*, *255*, 1687-1690, 1992.

Rothacher, M., G. Beutler, W. Gurtner, T. Schildknecht, and U. Wild, *Documentation for Bernese GPS Software Version 3.2*, Univ. of Bern, Bern, Switzerland, 1990.

Rundle, J.B., and D.D. Jackson, A three-dimensional viscoelastic model of a strike-slip fault, *Geophys. J. R. Astron. Soc.*, *49*, 575-591, 1977.

Rymer, M.J., Near-fault measurement of postseismic slip associated with the 1989 Loma Prieta, California, earthquake, *Geophys. Res. Lett.*, *17*, 1789-1792, 1990.

Savage, J.C., A theory of creep waves propagating along a transform fault, *J. Geophys. Res.*, *76*, 1954-1966, 1971.

Savage, J.C., and R.O. Burford, Accumulation of tectonic strain in California, *Bull. Seismol. Soc. Am.*, *60*, 1877-1896, 1970.

Savage, J.C., and M. Lisowski, Changes in long-term extension rates associated with the Morgan Hill and Loma Prieta earthquakes in California, *Geophys. Res. Lett.*, *22*, 759-762, 1995.

Savage, J.C., M. Lisowski, and J.L. Svarc, Postseismic deformation following the 1989 (M = 7.1) Loma Prieta, California, earthquake, *J. Geophys. Res.*, *99*, 13,757-13,765, 1994.

Savage, J.C., and W.H. Prescott, Asthenosphere readjustment and the earthquake cycle, *J. Geophys. Res.*, *83*, 3369-3376, 1978.

Scholz, C.H., A physical interpretation of the Haicheng earthquake prediction, *Nature*, *267*, 121-124, 1977.

Schwartz, S.Y., D.L. Orange, and R.S. Anderson, Complex fault interactions in a restraining bend on the San Andreas fault, southern Santa Cruz Mountains, California, *Geophys. Res. Lett.*, *17*, 1207-1210, 1990.

Shen, Z.K., D.D. Jackson, Y. Feng, M. Cline, M. Kim, P. Fang, and Y. Bock, Postseismic deformation following the Landers earthquake, California, 28 June 1992, *Bull. Seismol. Soc. Am.*, *84*, 780-791, 1994.

Smith, S.W., and M. Wyss, Displacement on the San Andreas fault subsequent to the 1966 Parkfield earthquake, *Bull. Seismol. Soc. Am.*, *58*, 1955-1973, 1968.

Snay, R.A., H.C. Neugebauer, and W.H. Prescott, Horizontal deformation associated with the Loma Prieta earthquake, *Bull. Seismol. Soc. Am.*, *81*, 1647-1659, 1991.

Steidl, J.H., R.J. Archuleta, and S.H. Hartzell, Rupture history of the 1989 Loma Prieta, California, earthquake, *Bull. Seismol. Soc. Am.*, *81*, 1573-1602, 1991.

Stein, R.S., Discrimination of tectonic displacement from slope-dependent errors in geodetic leveling from southern California, 1953-1979, in *Earthquake Prediction: An International Review, Maurice Ewing Ser.*, vol. 4, edited by D.W. Simpson and P.G. Richards,pp. 441-456, AGU, Washington, D.C., 1981.

Thatcher, W., Strain release mechanism of the 1906 San Francisco earthquake, *Science*, *184*, 1283-1285, 1974.

Thatcher, W., Nonlinear strain buildup and the earthquake cycle on the San Andreas fault, *J. Geophys. Res.*, *88*, 5893-5902, 1983.

Thatcher, W., Cyclic deformation related to great earthquakes at plate boundaries, in *Recent Crustal Movements of the Pacific Region*, Bull. Roy. Soc. N. Ze., Wellington, New Zealand, 245-272, 1986.

Toksöz, M.N., A.F. Shakal, and A.J. Michael, Space-time migration of earthquakes along the North Anatolian fault zone and seismic gaps, *Pure. Appl. Geophys.*,*117*, 1258-1270, 1979.

Tuttle, M.P., and L.R. Sykes, Re-evaluation of several large historic earthquakes in the vicinity of the Loma Prieta and Peninsular segments of the San Andreas fault, California, *Bull. Seismol. Soc. Am.*, *82*, 1802-1820, 1992.

Wald, D.J., D.V. Helmberger, and T.H. Heaton, Rupture model of the 1989 Loma Prieta earthquake from the inversion of strong-motion and broadband teleseismic data, *Bull. Seismol. Soc. Am.*, *81*, 1540-1572, 1991.

Williams, C.R., T. Arnadottir, and P. Segall, Coseismic deformation and dislocation models of the 1989 Loma Prieta earthquake derived from Global Positioning System measurements, *J. Geophys. Res.*, *98*, 4567-4578, 1993.

Wood, M.D., and S.S. Allen, Recurrence of seismic migrations along the central California segment of the San Andreas fault system, *Nature*, *244*, 213-215, 1973.

Yu, E., and P. Segall, Slip in the 1868 Hayward earthquake from the analysis of historical triangulation data, *J. Geophys. Res.*, *101*, 16,101-16,118, 1996.

R. Bürgmann, Department of Geology, University of California, Davis, CA 95616. (e-mail: burgmann@geology.ucdavis.edu)

M. Lisowski, Hawaiian Volcano Observatory, U.S. Geological Survey, Hawaii National Park, HI 96718. (e-mail: lisowski@usgs.gov)

P. Segall, Department of Geophysics, Stanford University, Stanford, CA 94305. (e-mail: segall@halape.stanford.edu)

J. Svarc, U.S. Geological Survey, Menlo Park, CA 94025. (e-mail: jsvarc@isdmnl.wr.usgs.gov)

(Received May 16, 1996; revised September 27, 1996;
accepted October 14, 1996)